Predicting Distal Radius Failure Load during a Fall using Mechanical Testing and Peripheral Quantitative Computed Tomography

A Thesis Submitted to the College of
Graduate and Postdoctoral Studies
in Partial Fulfillment of the Requirements
for the Degree
of Master of Science
in the Department of Mechanical Engineering
University of Saskatchewan
Saskatoon

By
Matthew Peter M^{c}Donald

Permission to Use

In presenting this thesis in partial fulfillment of the requirements for a Postgraduate degree from the University of Saskatchewan, I agree that the Libraries of this University may make it freely available for inspection. I further agree that permission for copying of this thesis in any manner, in whole or in part, for scholarly purposes may be granted by the professor or professors who supervised my thesis work or, in their absence, by the Head of the Department or the Dean of the College in which my thesis work was done. It is understood that any copying or publication or use of this thesis or parts thereof for financial gain shall not be allowed without my written permission. It is also understood that due recognition shall be given to me and to the University of Saskatchewan in any scholarly use which may be made of any material in my thesis.

Disclaimer

Reference in this thesis to any specific commercial products, process, or service by trade name, trademark, manufacturer, or otherwise, does not constitute or imply its endorsement, recommendation, or favoring by the University of Saskatchewan. The views and opinions of the author expressed herein do not state or reflect those of the University of Saskatchewan, and shall not be used for advertising or product endorsement purposes.

Requests for permission to copy or to make other uses of materials in this thesis in whole or part should be addressed to:

Head of the Department of Mechanical Engineering
University of Saskatchewan
57 Campus Drive
Saskatoon, Saskatchewan S7N 5A9
Canada

OR

Dean
College of Graduate and Postdoctoral Studies
University of Saskatchewan
107 Administration Place
Saskatoon, Saskatchewan S7N 5A2
Canada

Abstract

Distal radius fractures are the most common form of osteoporotic fracture in women and play an important role in predicting other osteoporotic fractures. Colles' fracture, a type of DRF, result from a fall from standing height or less. Peripheral quantitative computed tomography (pQCT) imaging is commonly used to estimate distal radius strength (resistance to failure) via bone strength indices such as BSI_c (related to compressive axial loading resistance). BSI_c has been validated in experimental compressive testing. However, during a fall, the distal radius is subjected to a combination of dorsal-directed forces (which result in bending) and axial compression. The primary objective of this study was to validate new pQCT-based bone strength indices combining resistance to bending and compression using optimized and clinically-applied image resolutions. The secondary objective was to validate these new indices against reported bone strength indices and bone properties for predicting the failure load in a mechanical testing scenario representing a fall on the extended hand.

Fourteen cadaveric forearms, with the hand intact, were scanned using pQCT at 4% of the length of the radius away from the distal end. Bone was defined as pixels with density > 100 mg/cm^3 and cortical bone as pixels with density > 480 mg/cm^3 using BoneJ, a tool designed to be used with ImageJ, an open source image analysis tool. This thresholding provided the basis for various measures which have been used in existing literature to predict failure load. Novel bone strength indices were calculated using composite beam theory based on the density of each pixel using total bone area, total volumetric bone mineral density and a density weighted modulus. Each of the novel measures examined the point of maximum stress in a single direction; this combined the uniform axial load applied over the cross-section and the bending resulting from an off-axis load, like that experienced during a fall. After scanning, potted samples were placed in a material testing system (MTS Bionix) with 15° of dorsal inclination and 3-6° of radial inclination, corresponding with the hand positon during a fall. Testing was performed at 3mm/s (180 mm/min) until fracture occurred and ultimate failure load was recorded. Linear regression models were used to assess imaged-based bone strength indices and bone properties predicting variance (coefficient of determination, R^2) in the experimentally derived failure load. A new bone strength index BSI_M, bone strength index in medial direction - which considered axial loading and bending stresses at the farther medial point on the radius, explained up to 90% of variance in the experimental failure load. The highest coefficient of

determination from metrics used previously in the literature was total bone mineral content (R^2 = 0.88). Two other novel bone strength indices, BSI_V (farthest point in the volar direction) and BSI_D (farthest point in the dorsal direction) predicted 88% of variance. Additionally, BSI_L (farthest point in the lateral direction) explained 86% of variance. This validates the use of these new measures as predictors of failure load in the distal radius during a fall. This work also found the existing measure of bone strength index in compression, BSI_c, predicted up to 83% of variance in the experimental failure load, which validates its use on the radius instead of remaining as a tibia specific tool.

Acknowledgements

I would like to extend my most sincere gratitude to my supervisors Dr. J.D. Johnston and Dr. Saija Kontulainen. Your expert guidance and seemingly never ending patience helped make this project what it is today and my experience during my program both very valuable and an absolute pleasure.

I would also like to express my gratitude to my advisory committee members. Dr. Geoff Johnston for his guidance with this project and Dr. Allan Dolovich for his help with working through composite beam theory's application to this project and for the valuable teaching opportunities he provided to me while pursuing a Master's degree.

I wish to express gratitude to the Saskatchewan Health Research Foundation and Natural Sciences and Engineering Research Council of Canada for providing such an excellent opportunity by funding this work.

It has been a treat to work with the research group, thank you all for the support, insight and help in this project. I will not soon forget the many late nights we spent together.

Thank you to my roommates and friends from all walks of life for helping to maintain my sanity. Endless gratitude goes to Anthony for always reminding me that life's swinging hard, but we're swinging harder.

Most of all, I want to thank my family. The compass may pull us in different directions but you taught me how to navigate this world with hope and heart. Thank you to my grandparents for all of their guidance and to Ron for being with me every step of the way. Mom and Dad, this thesis would not have been possible without your love and support.

Dedication

I'd like to dedicate this thesis to my grandfather, Albert Koenderink. I have no doubt that the time we spent together in your workshop gave me the passion that I have for all things mechanical.

Table of Contents

Permission to Use i
Disclaimer i
Abstract ii
Acknowledgements iv
Dedication v
Table of Contents vi
List of Tables viii
List of Figures ix
List of Abbreviations and Symbols xi
Glossary xiii
1. Introduction 1
    1.1. Overview 1
    1.2. Objectives 2
    1.3. Scope 2
2. Literature Review 4
    2.1. Functional Anatomy 4
    2.2. Colles' Fracture 8
    2.3. Osteoporosis 10
    2.4. Existing Tools 10
    2.5. Existing Methods to Predict Distal Radius Failure Load 12
    2.6. Summary 20
3. Methodology 22
    3.1. Cadaveric Specimens 22
    3.2. Specimen Preparation 22
    3.3. pQCT Imaging 25
    3.4. Image Analysis 26
    3.5. Model Development – Beam Theory 27
    3.6. Model Validation – Mechanical Testing 33
    3.7. Statistics 37
4. Results 38

5. Discussion 44
5.1. Bone Strength Index in Lateral Direction - BSI_L 45
5.2. Bone Strength Index in Volar Direction - BSI_V 45
5.3. Bone Strength Index in Dorsal Direction - BSI_D 46
5.4. Bone Strength Index in Medial Direction – BSI_M 46
5.5. Summary 46
5.6. Strengths and Limitations 46
6. Conclusions and Future Directions 49
6.1. Conclusions 49
6.2. Contributions 49
6.3. Clinical Significance 50
6.4. Recommendations for Future Research 50
References 52
Appendix A - Mechanical Testing Raw Data 58
Appendix B - Strain Gauge Mounting Protocol 72

List of Tables

Table 2.1: Coefficients of Determination (R^2) for Predicting Failure Load from DXA for a Fall Scenario from Distal Scan Site 13

Table 2.2: Coefficients of Determination (R^2) for Predicting Failure Load in a Fall Scenario 16

Table 4.1: Summary of BoneJ Results..... 39

Table 4.2: BoneJ Analysis Data..... 40

Table 4.3: Linear regression coefficients of determination (R^2) between experimentally measured failure load and image-based estimates of failure load..... 43

List of Figures

Figure 1.1: Dorsal View of Left Hand showing Carpal Bones [7] 4

Figure 1.2: Compressive Stress Transferred from Lunate/Scaphoid to Radius in Off-Axis Loading 5

Figure 1.3: Bending Moment Caused by Loading Location in Off-Axis Loading..... 6

Figure 1.4: Tensile Load Transmitted to Volar Side of Radius Through Ligaments in Off-Axis Loading 6

Figure 1.5: Free Body Diagram of Hand and Radius in off-axis loading..... 7

Figure 1.6: pQCT cross section of a) male left distal forearm (age 67) and b) female right distal forearm (age 101)..... 8

Figure 1.7: Colles Fracture Showing Dorsal Displacement of Distal End of Radius [14-15]..... 9

Figure 1.8: Off-axis loading broken down into axial compression and bending moment..... 10

Figure 1.9: Progression of Creating Subject Specific FE Model: a) Forearm, b) Forearm in a Scan Image & c) Development of FE model of Forearm Wrist Bones from Scan Image..... 13

Figure 1.10: Determining Area of Radius in BoneJ from pQCT Image..... 15

Figure 2.1: PMMA Hardening on Arm in Natural Fall Position 23

Figure 2.2: Lowering the Cut Forearm into the PVC 24

Figure 2.3: Radius and Ulna in Potting..... 24

Figure 2.4: Stratec XCT 2000 pQCT Scanner 25

Figure 2.5: Scan of 4% Site of Radius with 0.4 mm Pixel Size 26

Figure 2.6: Visual Results of pQCT Distribution Analysis Thresholding in BoneJ Showing Cortical bone in Cyan, Trabecular Bone in Magenta) 27

Figure 2.7: Directions for Bone Strength Indices on a pQCT Scan of the Radius 27

Figure 2.8: xarm and yarm shown on pQCT Scan..... 29

Figure 2.9: MTS Bionix Servohydraulic Test System Model 370.02 33

Figure 2.10: Specimen Mounted in MTS Bionix Tester..... 34

Figure 2.11: Specimen Showing Colles' Fracture 35

Figure 2.12: Load Vs. Time Plot showing Ultimate Load and Sharp drop in Load Indicating Fracture (Minor change at 100 N of load was due to lag in the testing program) 36

Figure 4.1: Experimental vs. Predicted Failure Load from BSIM..... 41

Figure 4.2: Experimental vs. Predicted Failure Load from BSIL..... 41

Figure 4.3: Experimental vs. Predicted Failure Load from BSIV 42

Figure 4.4: Experimental vs. Predicted Failure Load from BSID 42
Figure A.1: Load versus Time Curve for Specimen 14-06029L 58
Figure A.2: Load versus Time Curve for Specimen 14-06059L 59
Figure A.3: Load versus Time Curve for Specimen 14-08067R 60
Figure A.4: Load versus Time Curve for Specimen 15-02039L 61
Figure A.5: Load versus Time Curve for Specimen 15-07012R 62
Figure A.6: Load versus Time Curve for Specimen 15-07037R 63
Figure A.7: Load versus Time Curve for Specimen 1538L 64
Figure A.8: Load versus Time Curve for Specimen 1539L 65
Figure A.9: Load versus Time Curve for Specimen 1546L 66
Figure A.10: Load versus Time Curve for Specimen 1561R 67
Figure A.11: Load versus Time Curve for Specimen 1564R 68
Figure A.12: Load versus Time Curve for Specimen 1567L 69
Figure A.13: Load versus Time Curve for Specimen 1568R 70
Figure A.14: Load versus Time Curve for Specimen BR 71
Figure B.1: Strain Gauge Mounting Locations 72

List of Abbreviations and Symbols

Abbreviation/Symbol	Definition
θ	Angle of Radius in Mechanical Test Set-Up [°]
aBMD	Areal Bone Mineral Density [g/cm^2]
BMC	Bone Mineral Content [g]
A_w	Weighted Area [m^2]
BSI_c	Bone Strength Index – Compression [N]
BSI_V	Bone Strength Index – Combined Loading in Volar Direction [N]
BSI_D	Bone Strength Index – Combined Loading in Dorsal Direction [N]
BSI_M	Bone Strength Index – Combined Loading in Medial Direction [N]
BSI_L	Bone Strength Index – Combined Loading in Lateral Direction [N]
CoA	Cortical Bone Area [mm^2]
CoC	Cortical Bone Mineral Content [g/cm]
CoD	Cortical Bone Mineral Density [mg/cm^3]
DAQ	Data Acquisition System
DXA	Dual-energy X-ray Absorptiometry
F	Force to cause Colles' Fracture [N]
I_{max}	Area Moment of Inertia in the Maximum Direction [mm^4]
I_{min}	Area Moment of Inertia in the Minimum Direction [mm^4]
I_p	Polar moment of inertia [mm^4]
PMMA	Poly(Methyl Methacrylate)
pQCT	Peripheral Quantitative Computed Tomography
PVC	Polyvinyl Chloride
QCT	Quantitative Computed Tomography
R^2	Coefficient of Determination

S_c	Material Strength in Compression [MPa]
S_T	Material Strength in Tension [MPa]
SD	Standard Deviation
SSI	Stress-Strain Index [mm^3] – Density Weighted Modulus of Bone's Resistance to Bending
SSI_{max}	Stress-Strain Index in the Maximum Direction [mm^3]
SSI_{min}	Stress-Strain Index in the Minimum Direction [mm^3]
SSI_p	Stress-Strain Index in the Polar Direction [mm^3]
ToA	Total Bone Area [mm^2]
ToC	Total Bone Mineral Content [g/cm]
ToD	Total Bone Mineral Density [mg/cm^3]

Glossary

Term	Definition
Cortical Bone	Dense bone tissue forming outer shell of bone
Dorsal	Back side of a hand in neutral anatomical position
Distal	Direction toward the end of an extremity further away from the centre of a body
Ex vivo	Work performed outside of a living organism, such as tests performed on cadaveric specimens
In situ	Work performed in an environment simulating the natural conditions
In vivo	Work performed on or in a living organism
Lateral	Direction moving to the side from the centre of a body
Line of Action	Vector representing the direction in which a force is applied to a body
Medial	Direction moving from the side toward the centre of a body
Neutral Axis	A line running through an object which experiences no longitudinal stress or strain in bending
Proximal	Direction from the end of an extremity moving toward the centre of a body
Pixel Size	Dimension of each side of the smallest pixel element within an image
Trabecular Bone	Type of bone tissue comprised of vertical and horizontal trabeculae, small beam like structures, which create a spongy tissue; especially prevalent at the ends of long bones
Ultimate Load	Largest applied load reached in a sample during a destructive test
Volar	Direction toward the palm of the hand, also referred to as palmar
Voxel	Three dimensional element of space in an image
Yield Load	Applied load causing a stress where deformation in a material transitions from elastic to plastic and deformations become permanent

1. Introduction

1.1. Overview

Colles' fracture is a painful and common fracture of the distal radius, within the forearm, which typically occurs from a fall, from standing height or less, onto the outstretched hand [1-2]. There is an increased risk of fracture to people who suffer from osteoporosis, a degenerative bone disease where bone loses bone mineral density and experiences micro-architectural deterioration, leading to a weakened skeletal system [1]. This weakened skeletal system leaves people susceptible to fractures at much lower loads than people with healthy bones [2], and is especially prevalent in women over the age of 55 [5-6].

Colles' fractures are a major concern for the healthcare system in Canada and across the world. Colles' fractures account for approximately 25% of all bone injuries [3]. The prevalence of Colles' fractures is owed to the fracture being caused by a fall onto outstretched arms from standing height or less which occurs very frequently [4] [5].

There have been numerous studies which attempt to model the loads experienced by the distal radius in order to predict the load onto the hand which will cause failure. The overall aim of this field of research has been to predict Colles' fractures effectively in order to reduce their incidence in the real world. Modeling research has indicated that Colles' fractures can occur at lower loading magnitudes when the radius is loaded in an off-axis compression situation, which introduces both compressive and bending stresses, as opposed to the commonly assumed pure compressive situation [4]. Most previous research on modeling distal radius failure load has focused on a mathematical model which involves pure axial loading. There is a need for a mathematical model which considers both axial and bending stresses in the distal radius during an off-axis loading scenario.

A novel method utilizing pQCT (peripheral quantitative computed tomography) imaging technology, which considers both axial and bending stresses from an off-axis loading scenario, may be able to predict distal radius fracture load. pQCT takes a cross-sectional scan of an extremity. This scan provides geometrical information about the bones as well as the density distribution within the bones. This information can be utilized with composite beam theory in order to predict failure loads measured from mechanical testing of cadaveric forearms. This may provide an effective tool for monitoring bone strength. This model could then be applied non-invasively to patients in vivo and could be used to help predict fracture risk, particularly when

combined with existing methods to predict impact force arising from a fall onto the outstretch hand [6].

1.2. Objectives

The overall goal of this research is to develop and validate new bone strength indices to predict failure load causing Colles' fracture in vivo. Using imaged data with a combination of engineering-based composite beam theory and mechanical testing, the primary objective of this research was to develop new pQCT-based bone strength indices combining resistance to axial compression and off-axis bending. The secondary objective was to validate the new bone strength indices with respect to the prediction of the failure load obtained from mechanical tests representing a fall on the extended hand.

1.3. Scope

The main body of this paper includes how a novel method for predicting distal radius failure load was developed and evaluated. Chapter 2 is a review of some of the key concepts required for understanding the dynamics of Colles' fracture, some important details about how the set-up of any mechanical testing of the radius may affect the results and how osteoporosis plays a factor in the risk of fracture. Additionally, some of the metrics previously examined in the literature which have been used to predict distal radius fracture load are discussed in this chapter. Chapter 2 is about the main goal of this research, which is to develop and validate an effective model to predict Colles' fractures using parameters from a pQCT scan which could be applied non-invasively for patients in vivo. Chapter 3 contains details about the methodology utilized in this study for sample selection, for the mechanical testing and the image processing of the pQCT scan results. It also includes a discussion of how a model for off-axis compression would be developed from the results of the two. Chapter 4 contains the results of the mechanical testing, the values of some of the measures used previously in the literature from pQCT scan parameters and the statistical results for predicting failure load in the distal radius in off-axis compression. Chapter 5 is a discussion of the results of this study. This chapter has information about the predictive abilities of measures in this study relative to each other and the predictive abilities of the same measures in the literature. Additionally, specific strengths of this study and limitations which were faced in this work are outlined here. Chapter 6 includes conclusions which can be

drawn from this work and potential contributions this work may have to the field and to a clinical setting. It also contains potential for future research stemming from this work and for improvements that could be made based on the limitations of this study.

2. Literature Review

2.1. Functional Anatomy

2.1.1. Wrist Structure

An understanding of the anatomy of the forearm is necessary before one can begin thinking about mechanically testing. The shaft of the forearm contains two bones which run parallel along its length: the radius and the ulna. The radius is on the lateral side, the direction moving outward from the centre of the body, of the forearm in an anatomically neutral position, and is located proximal to the thumb. The ulna is on the medial side (the direction toward the centre of the body from the side) [7].

The radius and the ulna connect to a row of four carpal bones at the distal radiocarpal joint. This row of bones contains the scaphoid, lunate, triquetrum and pisiform, moving from lateral to medial. The radius articulates with the scaphoid and the lunate. There is a synovial membrane between the radius, ulna and the carpal bones which allows for motion of the hand and prevents damage to the bones during motion (Figure 2.1) [7].

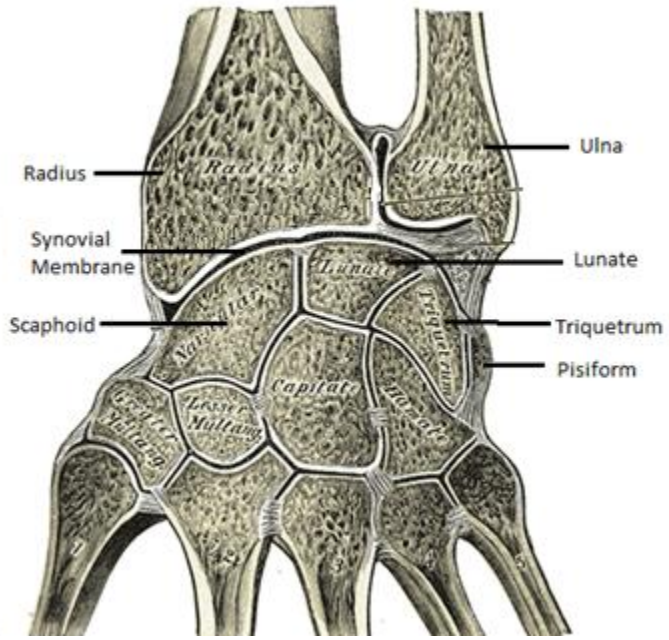

Figure 2.1: Dorsal View of Left Hand showing Carpal Bones [7]

Load applied to the hand will be transferred to the radius through these bones and the ligaments which connect them. The transfer of load from a fall onto an outstretched hand leads to three important loading conditions: compressive stress from off-axis, or eccentric, loading transmitted

through the lunate and scaphoid, bending stress from the eccentric location of the applied load relative to the longitudinal axis of the radius, and bending stress due to a tensile load transferred through the palmar ligaments attaching to the radius (Figure 2.2 – Figure 2.4). A free body diagram of this is shown in Figure 2.5.

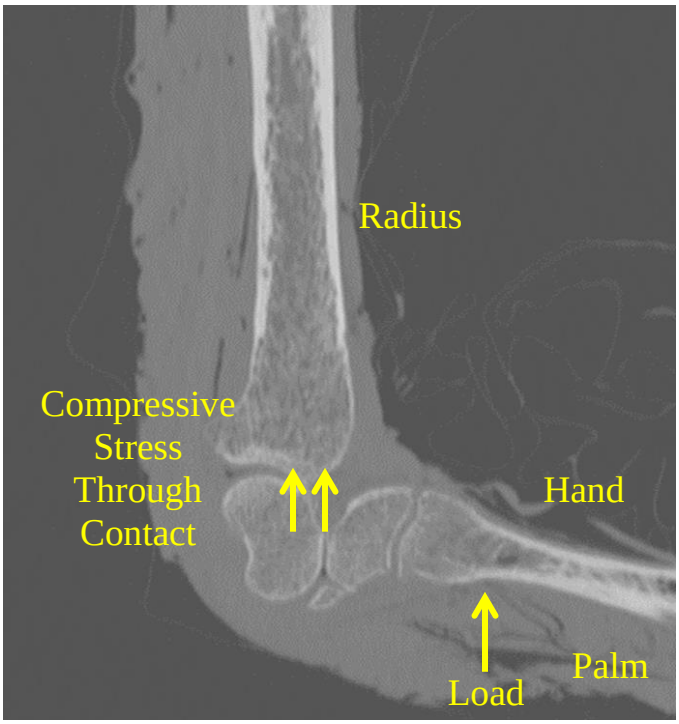

Figure 2.2: Compressive Stress Transferred from Lunate/Scaphoid to Radius in Off-Axis Loading

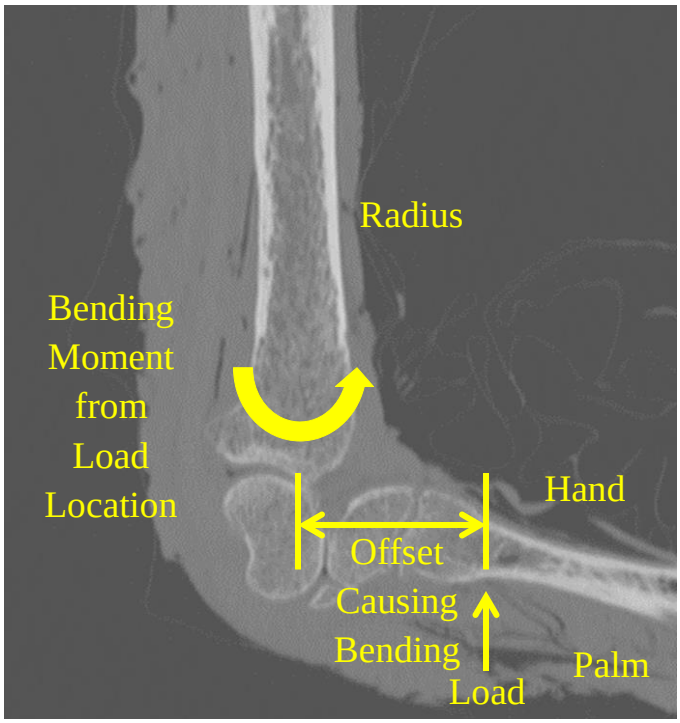

Figure 2.3: Bending Moment Caused by Loading Location in Off-Axis Loading

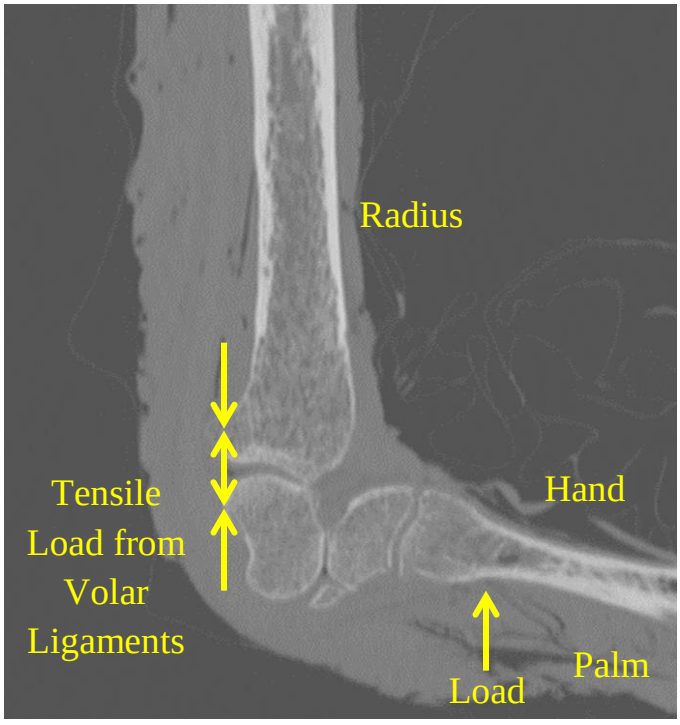

Figure 2.4: Tensile Load Transmitted to Volar Side of Radius Through Ligaments in Off-Axis Loading

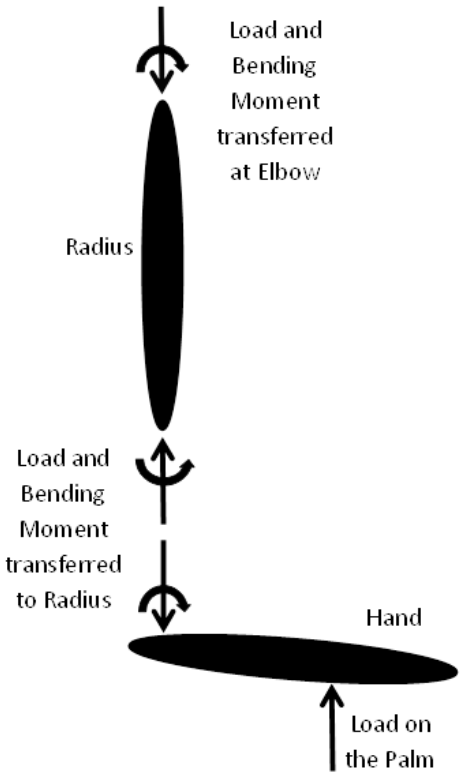

Figure 2.5: Free Body Diagram of Hand and Radius in off-axis loading

2.1.2. Bone Structure

Bones do not have a consistent structure throughout. The inner most structure of any bone is trabecular bone. Trabecular bone is highly porous and has a more lattice-like and spongy structure than the outer cortical region of bone. This lattice structure grows in response to external loading placed on the bone so that bones are best suited to the typical loading patterns they will face [8]. Cortical bone surrounds trabecular bone and is much denser but still maintains some porosity. [7] The extent of porosity can affect structural properties [9]. It can be difficult to determine an exact boundary between the two as the bone transitions between trabecular and cortical bone without a clearly defined boundary [10]. In Figure 2., a boundary appears much easier to define in a 67 year old male specimen when compared to a 101 year old female specimen, where the boundary between the cortical and trabecular bone appears more gradual. These images were taken at the 4% site of the radius. This site is 4% of the length of the radius proximal from the distal end of the bone. The periosteum is a coating which surrounds the

exterior of the cortical bone. Inside of the cortical shell and within trabecular bone is the medullary cavity which contains bone marrow (Figure 2.6) [7].

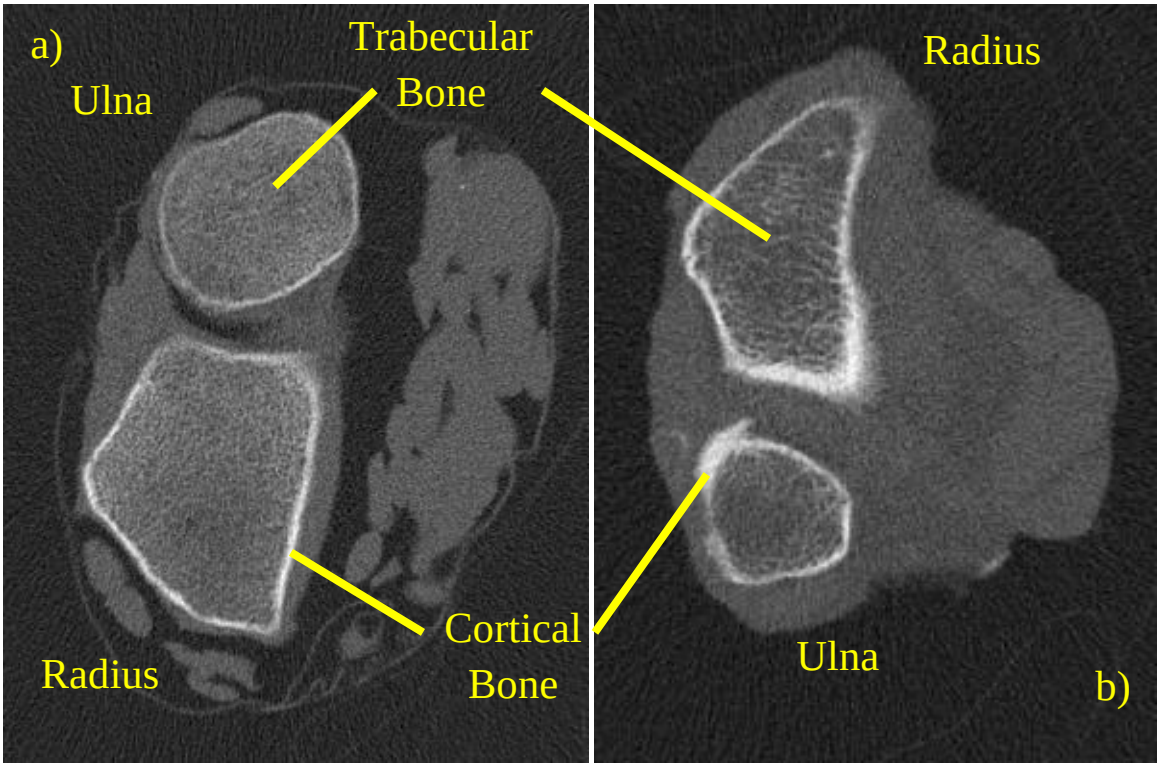

Figure 2.6: pQCT cross section of a) male left distal forearm (age 67) and b) female right distal forearm (age 101)

2.2. Colles' Fracture

Colles' fractures are marked by dorsal displacement of the distal end of the radius above a fracture site 1-2 cm proximal of this end [11]. A radiograph of a Colles' fracture is shown in Figure 2.7.

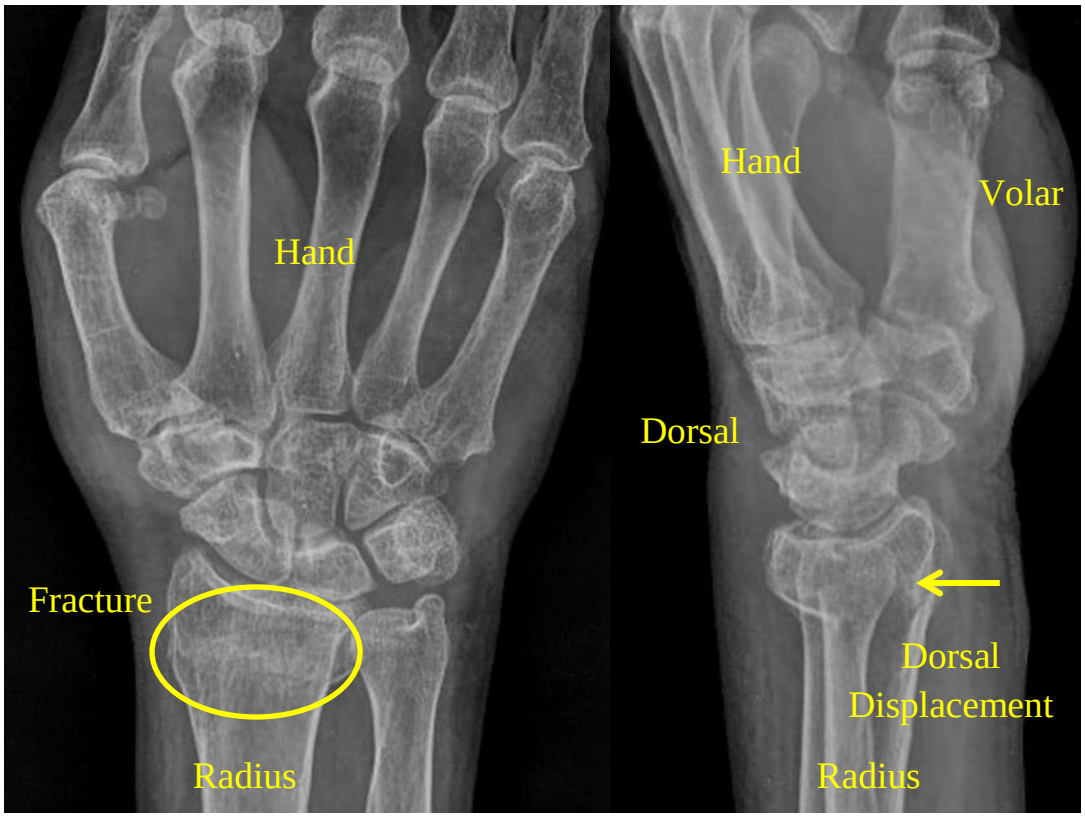

Figure 2.7: Colles Fracture Showing Dorsal Displacement of Distal End of Radius [14-15]

A Colles' fracture occurs when the external forces applied to the radius exceed the amount of stress that the forearm can handle. During a fall, the natural reaction is for a person to put their arms ahead as they fall forward to absorb the impact of the fall, which causes the impact forces to be applied onto the outstretched hand [12]. With this falling orientation, the radius is subjected to axial compression and bending, which causes volar (also referred to as palmar in this situation since this direction is toward the palm of the hand) tension and dorsal (the direction toward the back of the hand) compression [5].

Off-axis loading, or eccentric loading, can be broken down into two components: pure compressive loading and a bending moment (Figure 2.8). The simple compression component will cause a uniform compressive stress across the entire cross section of the bone. The bending moment will create a different stress based on the location within the cross section. This bending moment will create a tensile stress on the volar side of the radius and a compressive stress on the dorsal side of the radius as force is applied to an outstretched hand. This is important because cortical bone has a lower ultimate strength in tension than in compression [13].

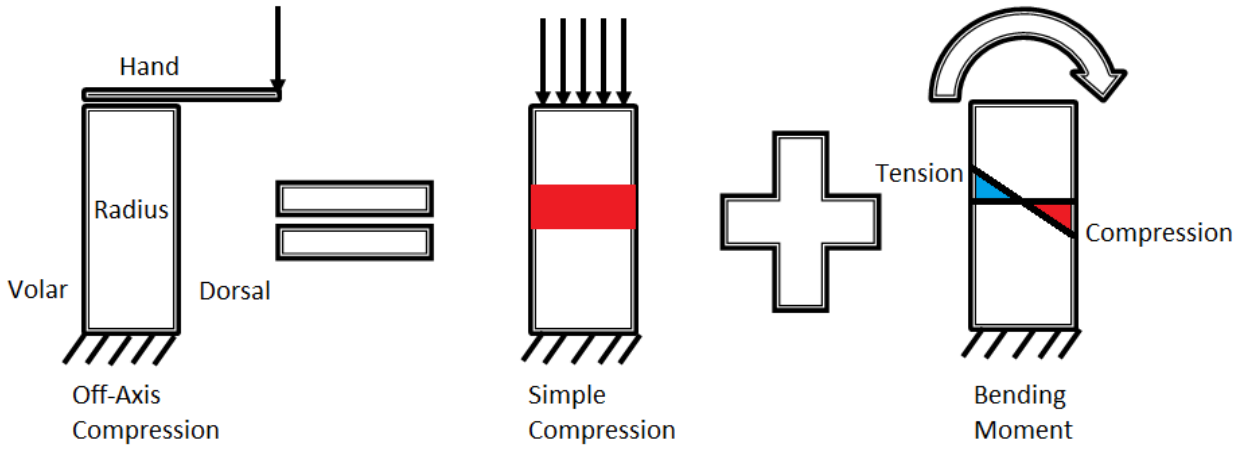

Figure 2.8: Off-axis loading broken down into axial compression and bending moment

2.3. Osteoporosis

In 2011, $4.6 billion was spent on dealing with osteoporosis and osteoporotic fractures in Canada [14]. Osteoporosis is defined as a multifactorial disease characterised by areal bone mineral density (aBMD) 2.5 times below the average for healthy young women [15] and micro-architectural deterioration leading to a weaker skeletal system [1]. This weakened skeletal system can lead to fractures with considerably less load than a healthy bone [2], which means that an increased risk of Colles' fracture has been linked to osteoporosis [16]. Osteoporosis affects women more than men, especially after menopause for women [1]. Colles' fracture serves as an important indicator of the risk of future fractures elsewhere on the body and it is also an early indicator for osteoporosis [17].

2.4. Existing Tools

2.4.1. Imaging

2.4.1.1. Peripheral Quantitative Computed Tomography

A pQCT scanner produces an image which contains the density of each pixel. This provides information about the distribution of cortical and trabecular bone as well as the porosity of cortical bone, which allows for determination of the structural properties of the bone, such as by using established correlations between Young's Modulus and bone mineral density (BMD) or correlating failure load with various measures such as bone mineral content (BMC), area

moment of inertia or total bone area [18]. The image also allows for calculation of both area and area moment of inertia of the bones, both of which are useful measures to determine resistance to off-axis loading encountered during a fall. It is important to note though that pQCT does not have sufficient resolution to provide information about the microstructure of trabecular bone. However, it has been shown that determination of bone microstructure does not improve bone strength predictions when testing entire bones to determine failure load [19]. A benefit of using pQCT for imaging is that there is a small radiation dose provided to patients. However, since pQCT provides only a small slice at the scanned location, so positional variation in repeated scans may influence outcomes [20].

2.4.1.2. High Resolution Peripheral Quantitative Computed Tomography

HR-pQCT has shown promise as a tool for evaluating mechanical properties of bone since it has the ability to measure BMD, bone micro-architecture and geometry of bones in three dimensions [21]. HR-pQCT can perform these measurement as it takes a series of slices along an extremity, which can be used to generate a three dimensional image, at a finer resolution than is available with standard pQCT. Unfortunately, this finer resolution and three dimensional imaging increases scan time and radiation dose to the patient. The longer scan times also increases the chance of a patient fidgeting which would cause movement errors in the scan images [20].

2.4.1.3. Dual Energy X-ray Absorptiometry

DXA scans have been used more for bone densitometry measurements than pQCT or HR-pQCT since scanners are more available [20]. DXA has the benefits of less sensitivity to movement than pQCT and a short scan time [20]. Unfortunately, DXA does not provide volumetric three dimensional BMD. Instead, it provides a two dimensional aBMD which brings uncertainty into the value due to patient positioning and size. This also means that DXA cannot provide information about the effects of bone size or bone mineral density distribution [21].

2.4.1.4. Quantitative Computed Tomography

QCT uses the same principles as pQCT or HR-pQCT but can be used at non-peripheral scan sites, such as the hip or spine. This type of imaging also provides BMD information and geometry information about bones without being affected by surrounding tissue or bone size like DXA [22].

2.5. Existing Methods to Predict Distal Radius Failure Load

2.5.1. Subject-Specific Finite Element Modeling

Subject-specific finite element, or FE, modeling has been used in previous work to predict distal radius mechanical behaviour and failure properties with models which were typically developed using Quantitative Computed Tomography, QCT, or HR-pQCT images. Finite element modeling involves developing a representation of a system which contains many small units, or finite elements, each representing a very small section of material being examined. Each of these elements can have their properties modeled in order to simulate an applied load or deflection to represent a real life scenario. Three-dimensional images acquired via QCT are required to develop a realistic representation of the geometry of a patient's bones. Also, QCT can be used to estimate bone's material properties due to established relationships between apparent density and strength and Young's modulus [23]. The performance of finite element models depends greatly on an accurate geometrical representation of the bones and material properties of the represented material being assigned appropriately [24]. Realistic loading and boundary conditions also need to be accurately applied to the finite element model for it to be able to predict a real life scenario effectively. To date, the majority of FE models of the distal radius only apply boundary conditions mimicking pure compressive testing and ignore the effects of bending. Nevertheless, subject-specific FE modeling has been able to predict failure loads in the radius quite successfully with R^2 values up to 0.98 for a small excised section of radius bone, instead of whole bones [25]. However, considerable time and care is required to develop an effective FE model since the prediction of failure load can vary considerably based on geometry and bone properties. It is not feasible to develop a general finite element model to apply to an entire population which can predict failure load for a particular patient effectively. This limits the applicability of finite-element modeling in a clinical setting. Figure 2.9 shows the progression as an FE model is developed.

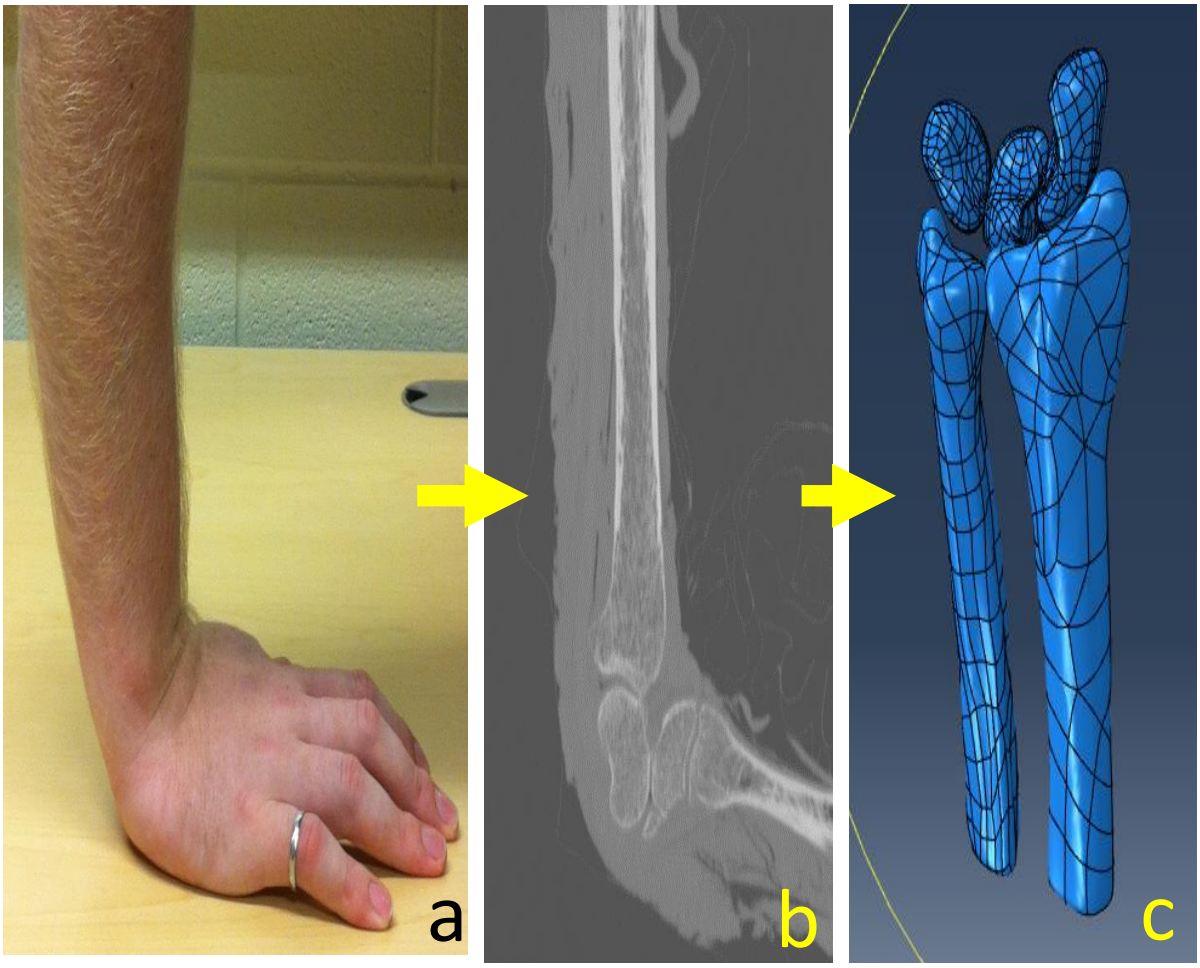

Figure 2.9: Progression of Creating Subject Specific FE Model: a) Forearm, b) Forearm in a Scan Image & c) Development of FE model of Forearm Wrist Bones from Scan Image

2.5.2. Dual Energy X-ray Absorptiometry

An overview of some of the measures acquired via DXA at the ultra-distal site, approximately a centimetre from the distal end, is listed below while their predictive abilities at estimating failure load are summarized here with their coefficients of determination summarized in Table 2.1.

Table 2.1: Coefficients of Determination (R^2) for Predicting Failure Load from DXA for a Fall Scenario from Distal Scan Site

Parameter	R^2
BMC [g]	0.53 [26]
aBMD [g/cm^2]	0.39 - 0.60 [18] [27]

2.5.2.1. Bone Mineral Content (BMC)

BMC refers to the sum of all bone mineral content in a scan. This measure does not provide any information about the geometry of the bones or the distribution of the mineral content. Using DXA to predict radial fracture in a fall scenario using BMC, measured at the ultra-distal radial site, was found to have a coefficient of variation of 0.53 [26].

2.5.2.2. Areal Bone Mineral Density (aBMD)

aBMD is a measure of the average density measured from a section identified as bone. DXA only scans a very small slice so bone mineral density can only be measured as a ratio of the bone mineral content divided by the area of the bone. This leads to some uncertainty in the measurement since density is a measure based on volume and not area. However, a coefficient of variation for predicting radial failure in a fall scenario using DXA scanning aBMD at the ultra-distal site of the radius was found to be 0.60 [18].

2.5.3. Peripheral Quantitative Computed Tomography - pQCT

pQCT has the advantage of providing information regarding bone mineral distributions and geometric properties, such as area and area moment of inertia [26]. The term peripheral comes from the fact that the machine is suited for imaging peripheral sites such as the distal radius and distal tibia. The radiation dose associated with pQCT is low, at less than 0.5 μSv per radial slice for a Strate XCT 2000L scanner [28].

The common pQCT imaging site associated with a Colle's fracture [5] is the 4% site of the radial length, measured proximal from the distal end of the bone. Scanning with pQCT provides useful information about the shape of the bones as well as the volumetric bone mineral density of each voxel within the image. Several studies have utilized densitometry scans in order to develop a model to predict distal radius failure load through measures of geometrical parameters such as area and area moment of inertia, derived from the pQCT image (Figure 2.).

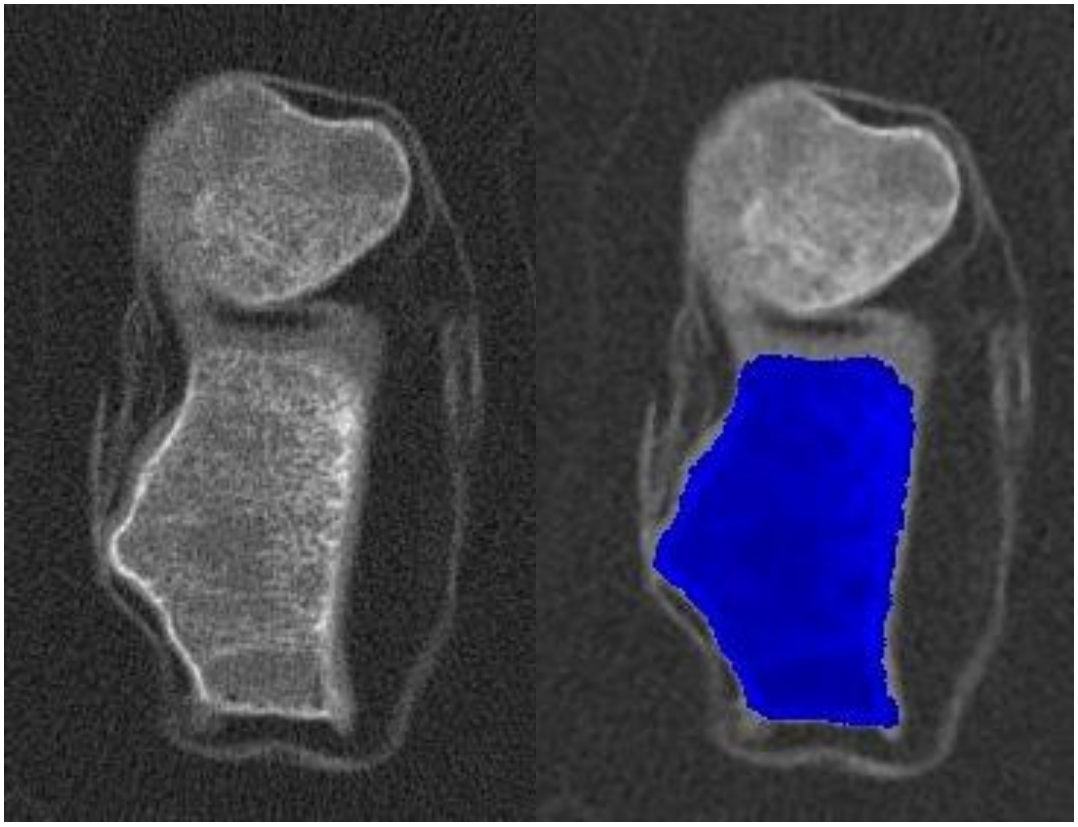

Figure 2.10: Determining Area of Radius in BoneJ from pQCT Image

This technique allows for a much simpler model than a FE model. This simplification allows for the creation of model that is more applicable to the general research environment since the time and knowledge required to use it are minimal. An overview of some of the measures is listed below while their predictive abilities at estimating failure load are summarized in Table 2.2.

Table 2.2: Coefficients of Determination (R^2) for Predicting Failure Load in a Fall Scenario

Parameter	R^2	Scan Site (% from distal end)
ToC [g/cm]	0.79 - 0.86 [18] [27] [31-32]	4
	0.53 – 0.69 [26]	5
CoC [g/cm]	0.64 – 0.85 [18] [29]	4
ToD [mg/cm^3]	0.47 – 0.76 [18] [27]	4
	0.56 [26]	5
CoD [mg/cm^3]	0.69 [18]	4
ToA [mm^2]	0.30 [18]	4
	0.50 [30]	10
CoA [mm^2]	0.24 [18]	4
I_{max} [mm^4]	Not Significant [18]	4
	0.55 [30]	10
I_{min} [mm^4]	0.53 [30]	10
I_p [mm^4]	0.58 [31]	20
SSI_{max} [mm^3]	0.25 [26]	5
SSI_{min} [mm^3]	0.30 [26]	5
SSI_p [mm^3]	0.85 [18]	4
	0.30 [26]	5

2.5.3.1. Total Bone Mineral Content

Total bone mineral content (ToC) is a measure of the entire bone mineral content above the minimum threshold set to be bone in a pQCT image. This value is not affected by the location of the bone mineral content and does not account for the geometry of the bone.

2.5.3.2. Cortical Bone Mineral Content

Cortical mineral bone content (CoC) is the sum of all mineral content above the minimum threshold defined for cortical bone in a scan. It provides a considerably different value from total bone content at the end site of long bones because they are highly trabecular. This value also does not reflect any influence from the bone geometry.

2.5.3.3. Total Volumetric Bone Mineral Density

Total volumetric bone mineral density (ToD) is an average of the total bone throughout an area of the scan identified as bone. This measure does take into account a volumetric density, which eliminates the uncertainty associated with aBMD taken from DXA measures.

2.5.3.4. Cortical Bone Mineral Density

Cortical bone mineral density (CoD) is very similar to ToD except that it is only applied to the pixels that have a measured density above a set threshold value for cortical bone.

2.5.3.5. Total Bone Area

Total bone area (ToA) is a measure of the entire cross-sectional region which has been determined to be above a minimum threshold of density to be considered as bone. This measure has an advantage of providing geometrical information about how the bone will resist axial compression but it lacks any information about bone mineral distribution which may be beneficial for a heterogeneous structure, like that of bone. In other words, a distal radius with thick cortical bone could have the same total area as a radius with thin cortical bone but more trabecular bone.

2.5.3.6. Area Moment of Inertia in the Maximum Direction

Area moment of inertia in the maximum direction, I_{max}, is a measure of resistance to bending in the direction where the bone has the most area. It is calculated by the summation of every pixel of bone being multiplied by the square of the distance from that pixel to the principal axis. The principal axis for I_{max} is in the volar-dorsal direction, with material located medially and laterally away from the principal axis included in the inertia measure. This measure considers the geometry of the bone in resistance to bending in one direction, which would be a bending

moment directed along the volar-dorsal axis at the radius. However, I_{max} does not consider the density of each pixel nor the resistance to axial loading.

2.5.3.7. Area Moment of Inertia in the Minimum Direction

Area moment of inertia I_{min}, is perpendicular to I_{max}. The principal axis for I_{min} points in the medial-lateral direction, with dorsal and volar material located away from the principal axis included in the inertia measure.

2.5.3.8. Polar Area Moment of Inertia

The polar area moment of inertia, I_p, is representation of how an object will resist torsion and it is the sum of I_{max} and I_{min}. For the radius, this is a measure of how it will resist torsion applied along the distal-proximal axis. To date, no pQCT studies have reported an associated between failure load and polar area moment of inertia measures at the 4% site of the distal radius.

2.5.3.9. Stress-Strain Index

The stress-strain index, SSI, is a density weighted modulus which represents a bone's resistance to bending. SSI is similar to the idea of the area moment of inertia in a particular direction, with adjustments for differences in density, and therefore Young's Modulus [23], akin to composite beam theory. Density weighting can be a large advantage as the area moment of inertia will treat a pixel of trabecular bone the same as a pixel of cortical bone if they are the same distance from the principal axis even though they would carry different amounts of load, as long as they are above the minimum threshold value for bone. Different types of bone structures carry different amounts of load because their elastic moduli differ greatly, with an elastic modulus for cortical bone around 16 GPa [32] while trabecular bone depends greatly on orientation but averages around 2 GPa along the length of the radius [33]. The SSI method was originally developed to account for partial volume effects at the outer cortical edge, but it also functions under the same principles as composite beam theory by adjusting for differences in elastic moduli. However, the model does assume a linear relationship between imaged bone density and elastic modulus whereas a number of studies have noted that elastic modulus has a power relation to bone mineral density [34]. In terms of outcomes, SSI_{max} represents the resistance to bending in the direction where SSI is the largest and SSI_{min} is the resistance to bending in the direction where

SSI is the smallest. With the radius, SSI_{min} is in the volar-dorsal direction and SSI_{max} is in the medial-lateral direction. SSI_p represents the polar SSI, which is the sum of SSI_{max} and SSI_{min}, and it can be used to estimate the ability of a radius to resist torsion applied along its proximal-distal direction. The equation is as follows:

$$SSI = \sum_{i=1,n} \frac{r_i^2 a \frac{density}{ND}}{r_{max}} \quad (2.1)$$

where r_{max} is the distance to the furthest voxel from the principal axis, density is the bone mineral density measure of each individual pixel, ND represents the normal density of cortical bone, treated to be 1200 mg/cm^3, r_i is the distance of the pixel to the principal axis, a is the area of the pixel and n is the number of pixels [35]. It is important to note that none of these methods account for bone's resistance to axial loading.

2.5.3.10. Bone Strength in Compression

Bone strength in compression, BSI_c, is a compressive strength index calculated by multiplying squared ToD by ToA [36]. BSI_c was created to estimate the failure load of a bone in compression. This measure has only been validated at the tibia with a coefficient of determination of 0.85 [37] but shows potential for use with the radius [36]. Validation of this index at the distal radius site would provide researchers with an additional tool to predict distal radius failure load in a fall scenario.

2.5.4. Mechanical Testing

2.5.4.1. Forearm Alignment

The alignment of the forearm bones during mechanical testing plays an important role in establishing a realistic failure load in an off-axis loading test. Several studies indicated that bending from off-axis loading would decrease the failure load by between 35% and 47% from a purely axial counterpart [4] [31] [38]. These studies indicated that if the testing alignment does not mimic physiologic conditions, then failure loads, derived from mechanical testing or modeling, would be much different than they would be in a real world scenario [4] [31] [38].

An important consideration for mechanical testing is that the hand must be allowed to dorsiflex as the load is being applied. The ligaments in the wrist transfer the bending stress along the volar side of the wrist as the hand is pulled back [4] which would be lost with a hand fixed in

place. The effects of the ligaments in an off-axis loading scenario in a living person may change the bone strength measure due to the potential stabilization effects of the ligaments [4].

2.5.4.2. Excised versus Intact Specimens

An issue associated with experimental validation studies is ensuring that the experimental and simulated boundary conditions match. One particular issue pertaining to this point is over-constraining tissue samples preventing a realistic fall scenario, which has occurred with key studies evaluating the mechanical properties of the distal radius [18] [27]. In this previous research, the excised distal radius was aligned at 10-15^{o} with the idea that off-axis loading and bending would be simulated, but the radius was constrained at both ends in potting material. When this set up was replicated, fractures characteristic of tensile loading on the volar side did not occur as expected [5] which may mean the tests induced purely compressive loading. By using forearms with an intact hand under a flat loading plate, the bone will be allowed to continue flexing during loading. The continued flexing of the hand replicates what would happen as a person falls onto their outstretch hands. Previous work has primarily utilized an excised radius for testing; however, ligaments and adjacent bones, scaphoid, lunate, trapezium and pisiform, in the wrist play an important role in properly transferring load, especially bending loads, to the forearm bones [5], so their inclusion, via an intact distal radiocarpal joint, during mechanical testing is warranted.

2.6. Summary

- Previous imaging and modeling research of the distal radius has focused predominately on axial loading type conditions whereas the wrist is subjected to a combination of axial compression and bending during a fall onto the outstretched hand.
- pQCT imaging is an established tool for predicting distal radius bone strength non-invasively. However, provided outcomes only consider pure bending, pure torsion or pure axial loading. None of the models integrate these different mechanical parameters to account for combined loading present when falling onto the hand.
- It is integral to keep the hand, wrist and distal end of forearm bones and the ligaments in the distal radiocarpal joint intact for mechanical testing to reflect a realistic falling scenario for a living person.

- The loading rate and hand position during a mechanical test are important because changes in either could affect the measured failure load significantly.

3. Methodology

3.1. Cadaveric Specimens

Twenty-seven (n=27) human forearm specimens were examined during testing for this research. All of these specimens were acquired from people who had consented to donating their body for research. Seventeen of the specimens were embalmed and the remainder were fresh-frozen at -20°C to preserve them until the time of testing. The fresh-frozen samples were thawed for approximately 20 hours before any preparation took place and then all preparation until testing occurred within 48 hours in order to refrain from unnecessary freeze-thaw cycles. Additionally, the ultimate strength, defined here to refer to the ultimate stress and not the failure load, of human cortical bone has been shown not to deteriorate significantly when tissue has been embalmed for up to 8 weeks [39]. It was expected that there would not be a significant difference between the embalmed and fresh-frozen samples used for this work; however, this was be evaluated as part of the analysis (see statistics section 3.7).

No age restrictions were in place for sample selection because this work was performed with the intention to develop a versatile model based on bone mineral density measures which reflect the effects of bone degradation during aging. Specimens were screened for any prior fractures or diseases, other than osteoporosis, which may affect bone mineral density measurements. Osteoporotic samples were not excluded since this work is most applicable to people who have suffered bone degradation from that very disease. There were seventeen females and eight males in the sample. Two specimens did not have information about the sex or age of the donor. The average age of the group was 81.4 years ± a SD of 9.1 years. There were fifteen left arms and twelve right arms that were tested. No information was provided about the hand dominance of the donor.

3.2. Specimen Preparation

The specimens were intact from the entire hand to midshaft of the humerus. The soft tissue surrounding the location where the potting material was attached was removed. First, the arms were placed in a falling orientation, which ensured that the radius and ulna were oriented correctly relative to one another. This is important because the radius actually spins around the ulna with different orientations of the hand and forearm, so this was a key step in ensuring correct boundary conditions and alignment of the hand during a fall. The ulna and radius were

then fixed in this orientated using a small amount of PMMA (Poly(methyl methacrylate)) placed around them in the area where the soft tissue had been removed. This was allowed to harden which then kept the bones locked in a natural falling position (Figure 3.1).

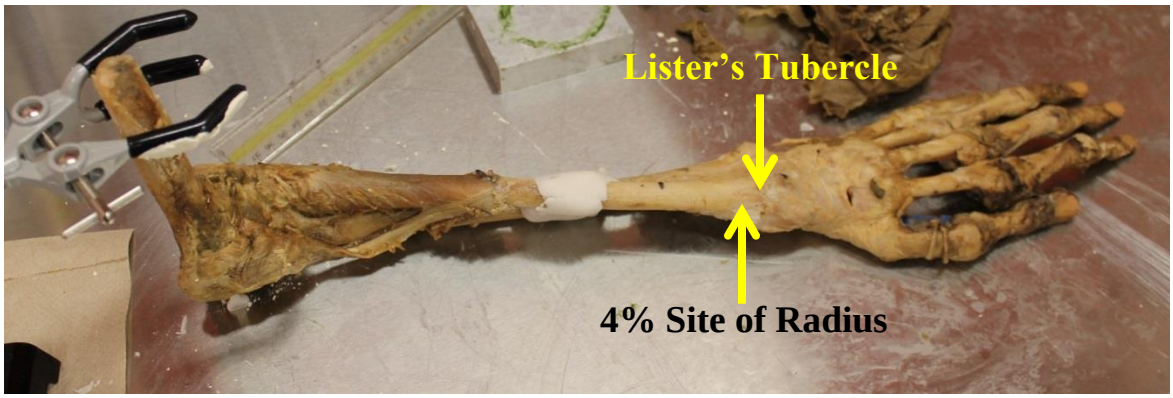

Figure 3.1: PMMA Hardening on Arm in Natural Fall Position

The radius and ulna were cut midshaft fourteen centimetres proximal of Lister's tubercle once the PMMA had hardened. Meanwhile, an 8 cm length of 2 inch diameter of PVC (Polyvinyl chloride) piping was cut and four holes were drilled around the sides at non-uniform heights and covered with painter's tape, these holes ensured that the potting would resist any torsion developed during testing and preventing spinning within the PVC pipe. The cut forearms were lowered into the centre of the PVC vertically and then filled with Denstone (a gypsum-based potting material) to approximately 7mm from the top of the PVC pipe, which was then allowed to harden for 20 minutes (Figure 3.2). A layer of PMMA was then added to the top of the potting to prevent moisture from reaching the Denstone base. In the end, the bones were potted with eight centimetres embedded in potting material, six centimetres proximal of Lister's tubercle (Figure 3.3) [40]. The specimens were kept moist with a spray bottle and towelettes using a saline solution during all sample preparation.

Figure 3.2: Lowering the Cut Forearm into the PVC

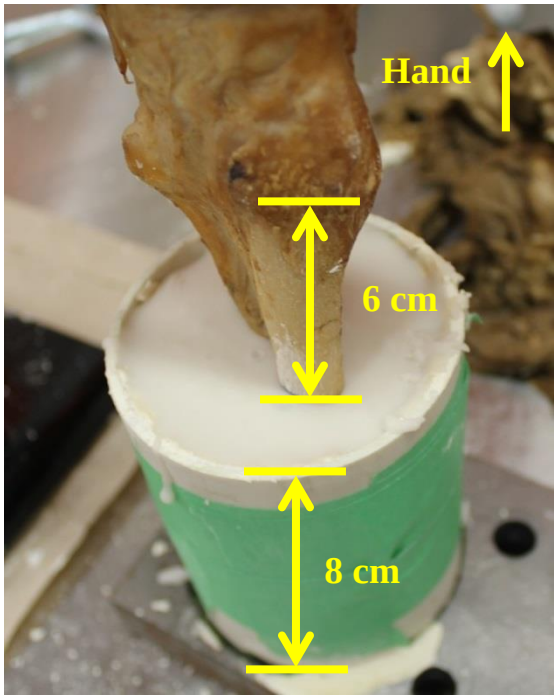

Figure 3.3: Radius and Ulna in Potting

3.3. pQCT Imaging

The specimens were imaged using pQCT (Stratec XCT 2000, Figure 3.4) following potting. The specimens were first imaged using a scout scan in order to determine exactly where to scan to image the site 4% of the length of the radius proximal from Lister's tubercle. Every sample had the 4% site scanned with an in-plane square pixel of 0.4 mm with a 2.4 mm ± 0.1 mm slice thickness (Figure 3.5). The 0.4 mm in-plane pixel size was indicative of common practice in the field [43-44].

Figure 3.4: Stratec XCT 2000 pQCT Scanner

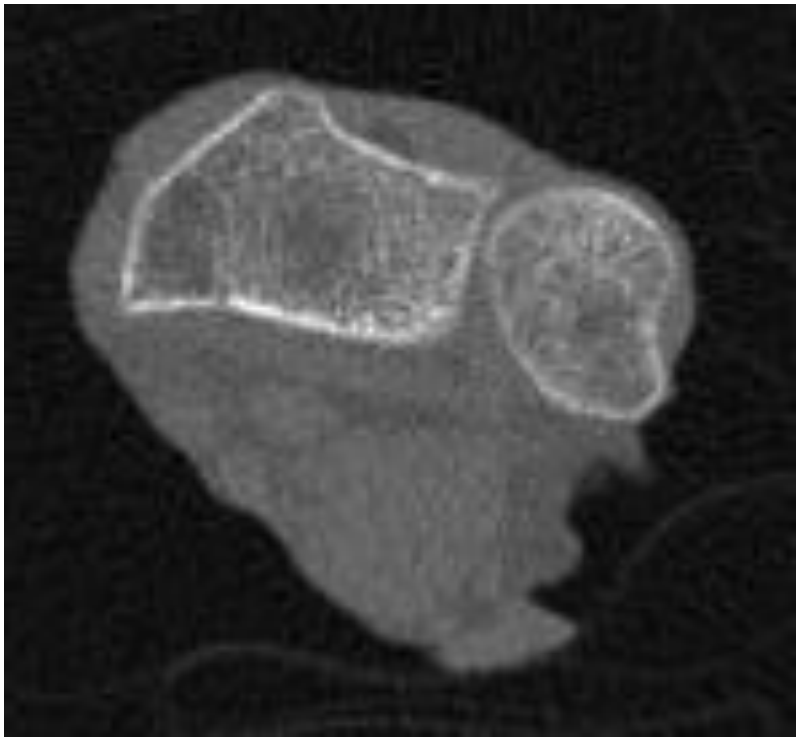

Figure 3.5: Scan of 4% Site of Radius with 0.4 mm Pixel Size

3.4. Image Analysis

Image analysis was performed on the pQCT scans using BoneJ, a bone imaging analysis plugin for ImageJ ((https://imagej.nih.gov/ij/) [41]. Both BoneJ and ImageJ are free, open source, image analysis software packages funded by the National Institutes of Health (NIH). A custom macro was created in order to process the images quickly. The macro used the 'analyze cortical results' functions in BoneJ to assess the geometric and density distribution properties of the bones from the pQCT image. This analysis was run using an area threshold to distinguish bone from soft tissue to be 100 mg/cm^3 and a density threshold of 480 mg/cm^3 to distinguish cortical bone from trabecular. The low values for the thresholds (lower than previously used values of 169 mg/cm^3 and 710 mg/cm^3 [27]) were chosen because higher values excluded large amounts of the trabecular region in some bones with low bone mineral density. The results from the analysis appeared in a window showing the geometric and density distribution properties, as well as an image showing the segmented trabecular and cortical regions, which was used to visually verify their accuracy (Figure 3.6).

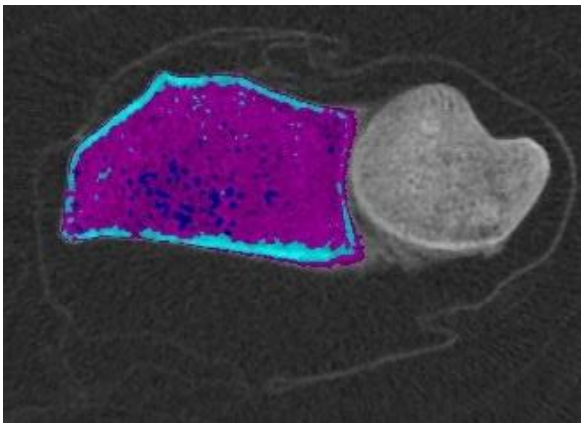

Figure 3.6: Visual Results of pQCT Distribution Analysis Thresholding in BoneJ Showing Cortical bone in Cyan, Trabecular Bone in Magenta)

This BoneJ analysis provided several measures commonly used in the literature for predicting failure load in the radius, which were mentioned earlier.

3.5. Model Development – Beam Theory

This section outlines how the equations used for bone strength indices in the volar, dorsal, medial and lateral directions were established. The coordinates relative to a pQCT scan can be seen in Figure 3.7. The principal axes are determined in BoneJ based on the shape of the radius.

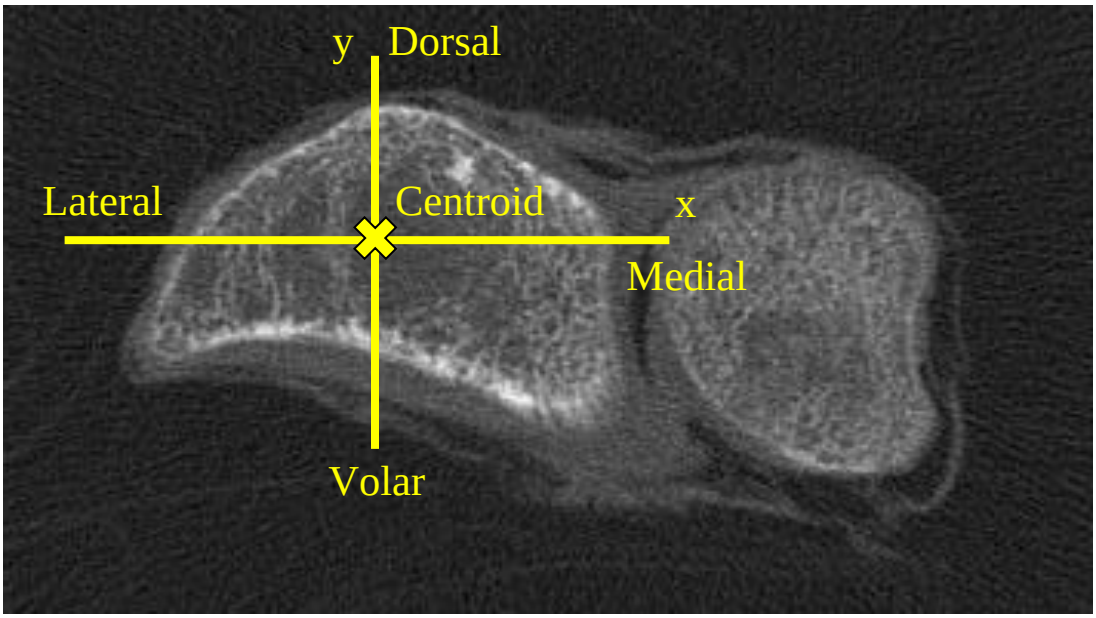

Figure 3.7: Directions for Bone Strength Indices on a pQCT Scan of the Radius

An equation from Rybicki et al. 1974 for strain at any point (x,y) on a bone which is experiencing off-axis loading:

$$\varepsilon = \varepsilon_0 + xk_y + yk_x \text{ [42]} \quad (3.1)$$

This equation uses ε to represent strain at a point of interest on a cross-section, ε_0 represents the strain from axial loading, x [m] is the distance from the centroid to the point in the x direction, k_y [m^{-1}] is the curvature of the bone about the y direction (equal to the reciprocal of the radius of curvature of the bone), y [m] is the distance from the centroid to the point in the y direction and k_x [m^{-1}] is the curvature of the beam about the x direction. This equation assumed that there was a linear strain distribution within the bone, that there would only be linear elastic behaviour during loading and neglected any effect of shear strain at the points. This equation incorporates all of the bending of the radius into two offset values. Hooke's law is used to change the strain terms to stress terms, with σ_{c+b} [Pa] representing total of compressive and bending stresses and σ_c [Pa] representing uniform axial stress:

$$\frac{\sigma_{c+b}}{E} = \frac{\sigma_c}{E} + xk_y + yk_x \quad (3.2)$$

The two curvature terms, k_x and k_y, are changed to terms involving bending moments using the equations:

$$k_x = \frac{M_x}{EI_x} \quad (3.3)$$

$$k_y = \frac{M_y}{EI_y} \quad (3.4)$$

Here, M_x [Nm] is the moment, acting about the x-axis, caused by the line of action of the applied force being located off of the centroid, M_y [Nm] is the moment, acting about the y-axis, caused by the line of action of the applied force being located off of the centroid, I_x [m^4] is the area moment of inertia which resists bending about the x axis and I_y [m^4] is the area moment of inertia which resists bending about the y axis. Combining equations 3.2 and 3.3 and 3.4 and eliminating E gives:

$$\sigma_{c+b} = \sigma_c + \frac{xM_y}{I_y} + \frac{yM_x}{I_x} \quad (3.5)$$

The axial compressive stress term is changed to force, F [N], per area, A [m^2] for a uniform axial compressive stress:

$$\sigma_{c+b} = \frac{F}{A} + \frac{xM_y}{I_y} + \frac{yM_x}{I_x} \tag{3.6}$$

Next, the bending moments are converted to the applied force multiplied by their respective offsets, represented by x_{arm} [m] and y_{arm} [m] for the offsets in the x and y directions (Figure 3.8):

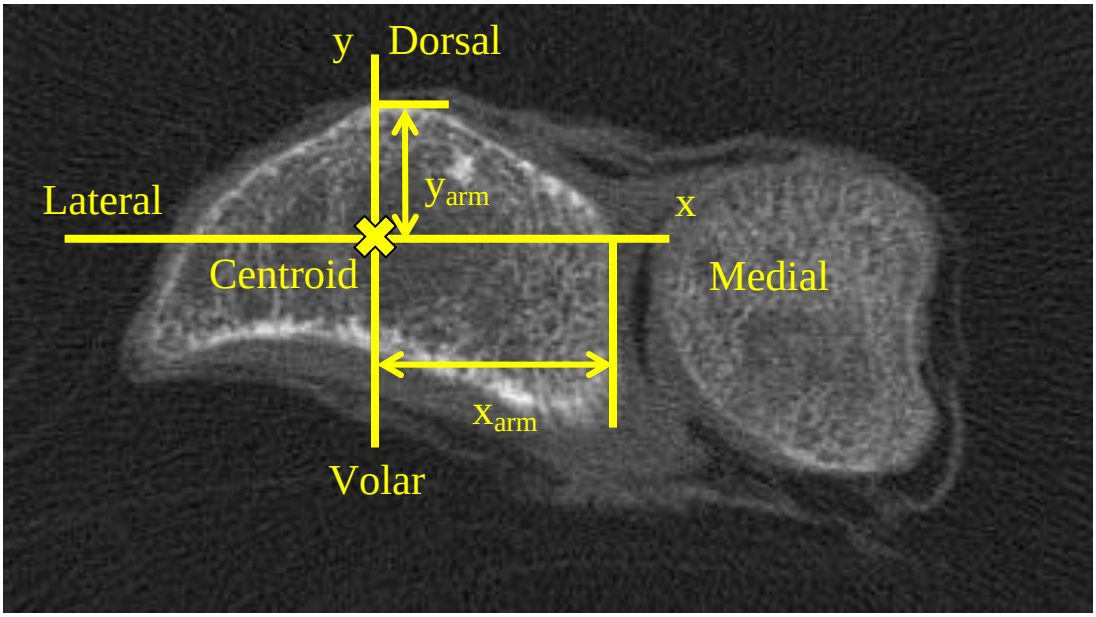

Figure 3.8: x_{arm} and y_{arm} shown on pQCT Scan

$$\sigma_{c+b} = \frac{F}{A} + \frac{x(Fx_{arm})}{I_y} + \frac{y(Fy_{arm})}{I_x} \tag{3.7}$$

Simplifying the right side of the equation, by extracting force from each term, gives:

$$\sigma_{c+b} = F\left(\frac{1}{A} + \frac{x(x_{arm})}{I_y} + \frac{y(y_{arm})}{I_x}\right) \tag{3.8}$$

The area moment of inertia terms are represented by their respective stress-strain indices multiplied by the distance from the centroid to the furthest point in the corresponding direction, x_{max} or y_{max}. Stress-strain indices represent a bone's resistance to bending about a particular axis and have the forms:

$$SSI_x = \sum_{i=1,n} \frac{y_i^2 a \frac{density}{ND}}{y_{max}} \quad (3.9)$$

$$SSI_y = \sum_{i=1,n} \frac{x_i^2 a \frac{density}{ND}}{x_{max}} \quad (3.10)$$

where x_i [m] and y_i [m] are the distance from the centroid to a specific pixel's x or y coordinate respectively, a [m^2] is the area of the pixel being examined, density [mg/cm^3] is the bone mineral density of the pixel being examined and x_{max} [m] and y_{max} [m] are the distances from the centroid to the furthest point in each direction. These stress-strain indices are similar to area moment of inertia except that each pixel's contribution is weighted based on its density and, like a section modulus, the entire index is divided by the furthest point in that direction from the centroid. The updated form of the total stress equation was:

$$\sigma_{c+b} = F\left(\frac{1}{A} + \frac{x(x_{arm})}{x_{max}SSI_y} + \frac{y(y_{arm})}{y_{max}SSI_x}\right) \quad (3.11)$$

The cross-sectional area, A, will be represented by the following equation which provides a weighted area measure which accounts for lower density pixels taking less load than a pure cortical pixel, with density of 1200 mg/cm^3 [35], using:

$$A_w = ToA\left(\frac{ToD}{ND}\right) \quad (3.12)$$

where ToA is the total cross sectional area and ToD is the total volumetric bone mineral density. This gives an updated version of the combined stress equation:

$$\sigma_{c+b} = F\left(\frac{ND}{ToA \cdot ToD} + \frac{x(x_{arm})}{x_{max}SSI_y} + \frac{y(y_{arm})}{y_{max}SSI_x}\right) \quad (3.13)$$

Solving for the applied force gives:

$$F = \frac{\sigma_{c+b}}{\left(\frac{ND}{ToA \cdot ToD} + \frac{x(x_{arm})}{x_{max}SSI_y} + \frac{y(y_{arm})}{y_{max}SSI_x}\right)} \quad (3.14)$$

This equation is the basis for the novel methods used in this study. Unfortunately, it is impossible to determine the exact location with the most severe loading from bending moments in both x and y directions in one equation. This means that four different bone strength index models have

to be developed to represent the maximum stress calculated with the force at the furthest point from the centroid in each of the volar, dorsal, medial and lateral directions.

3.5.1. Bone Strength Index in Dorsal Direction - BSI_D

The bending of the hand dorsally during testing was expected to produce a compressive bending stress on the dorsal side of the radius, in addition to the uniform axial stress across the entire cross-section. It was assumed that the dorsal side of the radius would fail in compression so the ultimate strength of the radius in compression of 18.1 MPa [43] was put in for the σ_{c+b} term. The second term on the left side will go to zero since no bending effects in the x-direction are being considered in this model. The parameter y will become y_{max} since the point of maximum stress in this direction will be the furthest point from the centroid in dorsal direction. Additionally, SSI_x was represented by SSI_{min} [m^3] since this is the name given to the term for stress-strain index about the medial-lateral axis from BoneJ. ND will be represented by 1200 mg/cm^3. Finally, F was be represented by BSI_D [N]. These changes gave the following form for BSI_D:

$$BSI_D = \frac{18.1}{\left(\frac{1200}{ToA * ToD} + \frac{yarm}{SSI_{min}}\right)} \tag{3.15}$$

3.5.2. Bone Strength Index in the Volar Direction - BSI_V

BSI_V [N] is very similar to BSI_D except that it focuses on the volar end of the volar-dorsal axis. This means the point examined will experience a compressive axial stress and a tensile bending stress instead of only compressive. The bending term is treated as negative with the absolute value of the offset value for simplicity. It was assumed that a net tensile stress would govern at this point so that the ultimate strength of the radius in tension was the critical property instead. Studies have shown that longitudinal femoral bone has a ratio of roughly 0.69 of the ultimate strength in tension than in compression [13] [44]- [45] but similar studies could not be found for the radius. Using this ratio with the compressive ultimate strength of 18.1 MPa [43], the tensile ultimate strength of the radius was estimated to be 12.5 MPa. The furthest point from the medial-lateral axis was on the dorsal side so the maximum distance on the volar side had to be expressed as a ratio of the maximum distance to the furthest dorsal point because SSI terms include the maximum distance whether it is on the side being examined or not. This ratio was

estimated to be 0.85 by measuring and averaging the maximum volar and dorsal distances in the scan images taken during this study. Additionally, since the bending term is in tension it had to be considered negative in this equation. This gave the equation for BSI_V to be:

$$BSI_V = \frac{12.5}{\left(\frac{1200}{ToA * ToD} - 0.85 \cdot \frac{|y_{arm}|}{SSI_{min}}\right)} \quad (3.16)$$

3.5.3. Bone Strength Index in the Lateral Direction - BSI_L

BSI_L [N] is similar to the two previous two measures except that it includes bending about the volar-dorsal axis instead of the medial-lateral axis, which means that SSI_{min} needed to be replaced by SSI_{max} [m^3] and y_{arm} needed to be replaced by x_{arm}. The mechanical testing set up introduced a small radial angle which would cause compression on the lateral side of the radius. However, the furthest lateral point was closer to the volar-dorsal axis than the further medial point so a ratio had to be introduced to the bending term, like that in BSI_V. However, the samples showed an average ratio of around 0.80 in this direction instead of the value of 0.85 used previously. These changes gave the following:

$$BSI_L = \frac{18.1}{\left(\left(\frac{1200}{ToA * ToD}\right) + \left(0.80 \cdot \frac{x_{arm}}{SSI_{max}}\right)\right)} \quad (3.17)$$

3.5.4. Bone Strength Index in the Medial Direction - BSI_M

BSI_M [N] is along the same axis as BSI_L but the opposite direction. Since this means it was on the other side of the centroid from the BSI_L, it had tensile bending stresses introduced instead of compressive. Additionally, the bending term is represented as negative for tension but the absolute value of the offset is taken for simplicity. The furthest point from the volar-dorsal axis was in the medial direction instead of lateral so no ratio needed to be applied for the maximum point. This meant that BSI_M had the following form:

$$BSI_M = \frac{12.5}{\left(\left(\frac{1200}{ToA * ToD}\right) - \frac{|x_{arm}|}{SSI_{max}}\right)} \quad (3.18)$$

3.6. Model Validation – Mechanical Testing

3.6.1. Overview

To evaluate the proposed models, this study employed a combination of experimental mechanical testing with cadaveric forearms, pQCT imaging analyses, engineering-based composite beam theory and regression analyses to identify appropriate x_{arm} and y_{arm} values for BSI_D, BSI_V, BSI_L and BSI_M. The relative appropriateness of the various indices was based upon largest coefficient of determination.

3.6.2. Mechanical Testing

Specimens underwent mechanical testing using a material testing system (MTS Bionix Servohydraulic Test System, Model 370.02) with a 25 kN load cell (Figure 3.9).

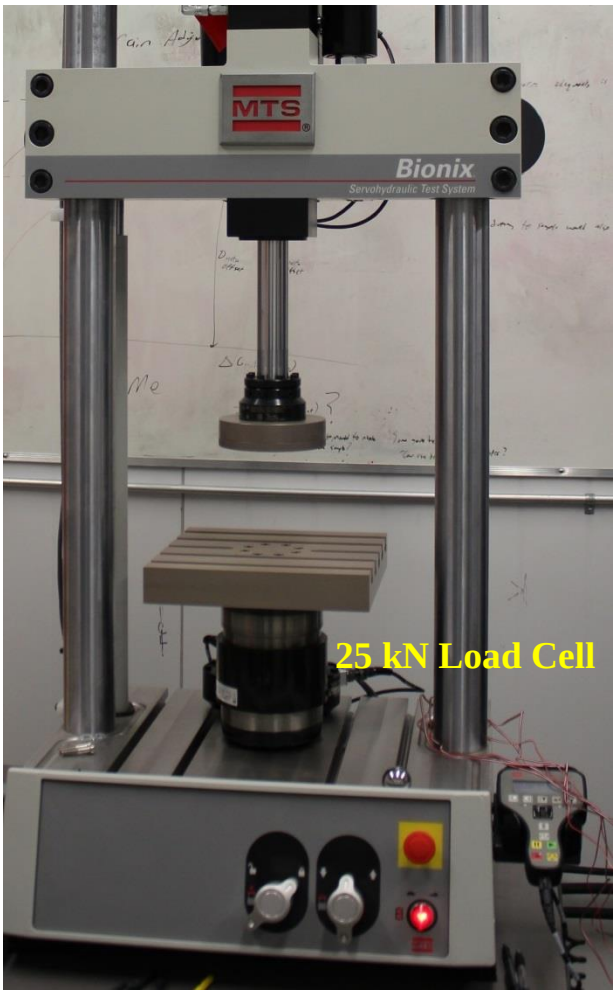

Figure 3.9: MTS Bionix Servohydraulic Test System Model 370.02

The specimens were mounted in an angled clamp at 15° of dorsal inclination [18]. A lateral inclination of 3°-6° was used for the palm to be flat against the loading plate; previous studies had used up to 10° [31] [46]. The dorsal inclination was needed in order to match the natural position of the arm in a falling scenario by introducing bending in an off-axis compression situation. The lateral inclination varied slightly because it was used to have the palm of the hand flat against the loading plate during the test in order to reduce lateral bending stresses resulting from the shape of the palm not being uniform (Figure 3.10).

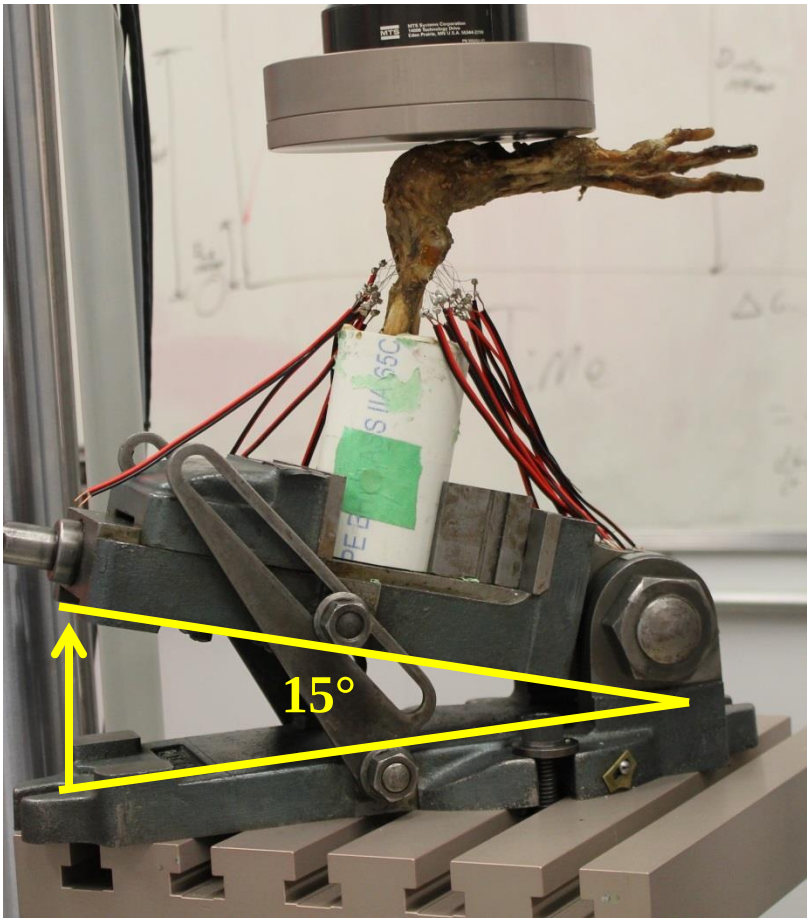

Figure 3.10: Specimen Mounted in MTS Bionix Tester

The loading plate was moved down against the specimen until a force of 40 N was detected in the load cell. The loading plate was then raised from this displacement to 4 mm upward and back down to the same displacement in order to apply a small repetitive load in a sine wave pattern at a rate of 0.5 Hz for five minutes. Applying this small “preconditioning” load, repeatedly, relaxed the soft tissue which allowed for smoother loading of specimen. The

Bionix test controller was connected to a data acquisition system (DAQ, National Instruments PXIe-1078 chassis with a PXIe-4300 voltage measurement) which recorded actuator displacement and load cell readings via a custom Labview program. Data was gathered at 1000 Hz. Strain data was also recorded for all of these tests, although the data was not used in this study. The protocol for mounting strain gauges is included in Appendix B.

After the preload cycles had run for 5 minutes, the specimens were tested to failure at a rate of 3 mm/second (180mm/min) similar to the 3.3 mm/second rate used previously [31]. After the specimen had fractured, a visual inspection was performed in order to verify that a Colles' fracture had occurred (Figure 3.11).

Figure 3.11: Specimen Showing Colles' Fracture

The plots of load against time were manually examined in order to determine the ultimate failure load. Fracture was visible in the plot due to either a sudden drop in force or a gradual decrease in force from the ultimate load, followed by a large drop (Figure 3.12).

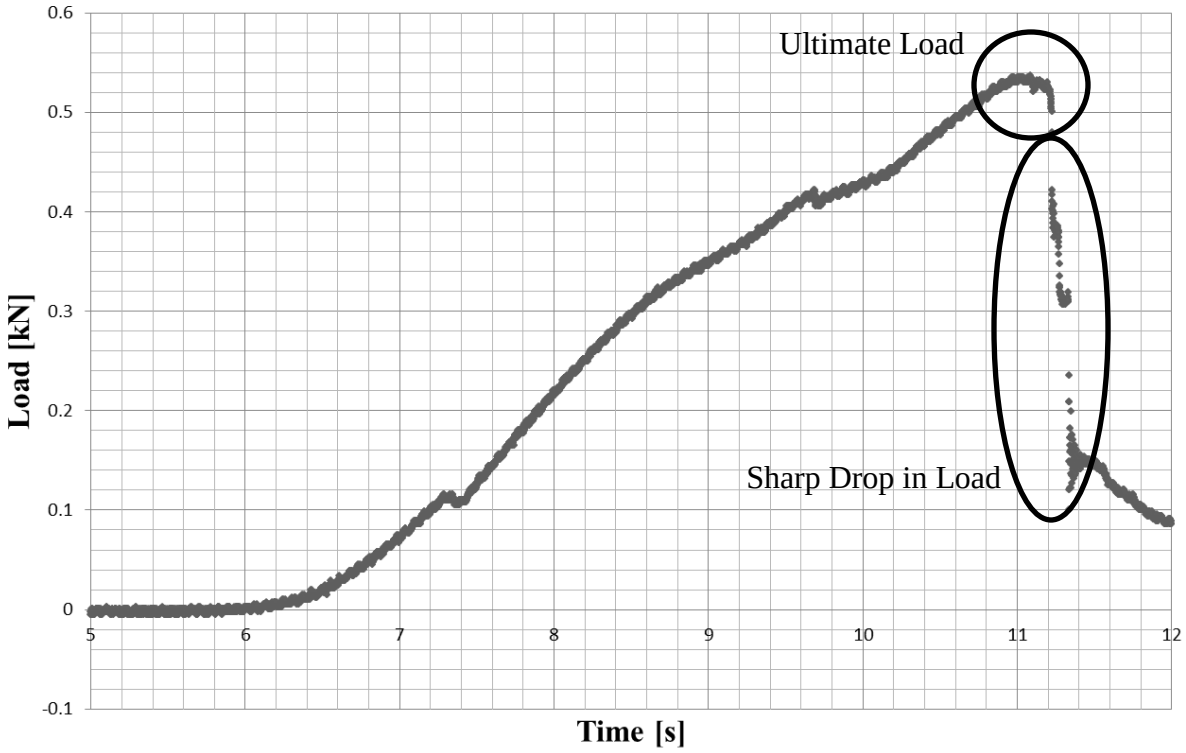

Figure 3.12: Load Vs. Time Plot showing Ultimate Load and Sharp drop in Load Indicating Fracture (Minor change at 100 N of load was due to lag in the testing program)

3.6.3. Model Evaluation

The new indices proposed to predict the force required to cause a Colles' fracture were evaluated. Different values of x_{arm} and y_{arm} were evaluated to identify the appropriate model which had the highest coefficient of determination, or R^2, from linear regression for each model.

$$F = BSI_D = \frac{18.1}{\left(\left(\frac{1200}{Total\ Area * Total\ Density}\right) + \frac{y_{arm}}{SSI_{min}}\right)} \quad (3.19)$$

$$F = BSI_V = \frac{12.5}{\left(\left(\frac{1200}{Total\ Area * Total\ Density}\right) - \left(0.85 * \frac{|y_{arm}|}{SSI_{min}}\right)\right)} \quad (3.20)$$

$$F = BSI_L = \frac{18.1}{\left(\left(\frac{1200}{Total\ Area * Total\ Density}\right) + \left(0.80 * \frac{x_{arm}}{SSI_{max}}\right)\right)} \quad (3.21)$$

$$F = BSI_M = \frac{12.5}{\left(\left(\frac{1200}{Total\ Area * Total\ Density}\right) - \frac{|x_{arm}|}{SSI_{max}}\right)} \quad (3.22)$$

3.7. Statistics

The relationship between experimentally-derived ultimate failure load and various bone metrics used previously (e.g., area, area moment of inertia) was examined. Additionally, the new strength indices of BSI_V, BSI_D, BSI_M, and BSI_L were assessed using linear regression and coefficients of determination (R^2) were compared when each index was used to predict to experimental failure load. For all models, a p value less than 0.05 was considered statistically significant when determining a difference between the measured and the observed values and allowed for rejecting the null hypothesis about a lack of relation between the two values.

4. Results

Thirteen of the samples were excluded from statistical analysis. Two of those thirteen showed signs of mold on the bones and were excluded. The other eleven specimens were excluded because they did not experience Colles' fracture during mechanical testing. Five of those eleven had the ligaments in the wrist compromised prior to testing as they had been used in an anatomy instruction lab. Two of the eleven were excluded because the loading could not be stopped quickly enough and it was impossible to verify the presence of a Colles' fracture. The other four of the eleven broke elsewhere on the radius, either at the edge of the potting or as a spiral fracture midshaft. Fourteen of the initial twenty-seven samples remained in for the statistical analysis. Six of these were fresh-frozen and the other eight had been embalmed.

Descriptive statistics for imaging outcomes pertaining to the fourteen evaluated specimens are found in Table 4.1. The average failure load from mechanical testing was 994 ± 548 N with a range of 427 to 2427 N.

Table 4.1: Summary of BoneJ Results.

Imaging Outcome	Mean ± SD (Range)
Total Density ToD (mg/cm^3)	247.8 ± 49.4 (172.0 – 376.4)
Cortical Density CoD (mg/cm^3)	684.4 ± 68.6 (547.4 – 779.7)
Total Area ToA (mm^2)	402.1 ± 58.7 (326.4 – 588.0)
Cortical Area CoA (mm^2)	29.2 ± 16.9 (3.36 – 65.6)
Area Moment of Inertia in Volar-Dorsal Direction I_{max} (mm^4)	19951 ± 5191 (13934 – 31079)
Area Moment of Inertia Medial-Lateral Direction I_{min} (mm^4)	8337 ± 4001 (5007 – 22141)
Polar moment of inertia I_p (mm^4)	288288 ± 8580 (18941 – 53221)
Strength Strain Index in Volar-Dorsal Direction SSI_{max} (mm^3)	279.5 ± 76.9 (179.5 – 430.3)
Strength Strain Index in Medial-Lateral Direction SSI_{min} (mm^3)	137.3 ± 57.9 (83.2 – 323.3)
Strength Strain Index in Polar Direction SSI_p (mm^3)	416.7 ± 124.9 (262.7 – 723.5)
Bone Strength Index in Compression BSI_c (mg^2/mm^4)	25.4 ± 10.8 (11.5 – 56.5)
Total Content ToC (g/cm)	0.99 ± 0.22 (0.67 – 1.50)
Cortical Content CoC (g/cm)	0.21 ± 0.13 (0.02 – 0.50)
BSI_M (N)	1420.7 ± 302.7 (971.7 – 2124.6)
BSI_L (N)	1229.8 ± 285.4 (823.1 – 1867.9)
BSI_V (N)	1050.4 ± 235.4 (709.0 – 1591.9)
BSI_D (N)	1468.9 ± 332.2 (989.3 – 2215.4)

Table 4.2 contains more detailed information about the boneJ parameters of each specimen as well as more details about the specimen.

Table 4.2: BoneJ Analysis Data

Patient Name	14-06029L	14-06059L	14-08067R	15-02039L	15-07012R	15-07037R	MT-1538L	MT-1539L	MT-1546L	MT-1561R	MT-1564R	MT-1567L	MT-1568R	MT-BR
Preservation	Frozen	Frozen	Frozen	Frozen	Frozen	Frozen	Embalmed	Embalmed	Embalmed	Embalmed	Embalmed	Embalmed	Embalmed	Embalmed
F Ultimate [N]	537	719	722	427	508	667	971	1774	961	1072	1458	489	2427	1187
Object Length [mm]	238	229	234	225	234	230	258	243	238	238	226	234	249	235
CoD (mg/cm3)	584.9	710.8	635.0	547.4	646.0	760.3	647.1	652.9	743.8	646.8	779.7	758.9	732.4	736.4
CoA (mm2)	8.3	24.5	25.0	3.4	14.6	65.6	26.4	28.0	35.5	15.2	42.6	30.7	58.9	30.2
SSIp (mm3)	301.3	341.4	357.9	262.7	328.6	363.1	451.8	723.5	504.9	326.1	474.5	324.1	604.8	469.8
SSImax (mm3)	208.8	218.6	241.7	179.5	222.8	259.2	310.8	400.2	380.4	209.0	301.5	224.5	430.3	325.0
SSImin (mm3)	92.5	122.8	116.1	83.2	105.8	103.9	140.9	323.3	124.5	117.1	173.0	99.6	174.5	144.8
Ip (mm4)	24053	26601	28077	23099	23792	18941	34226	53220	35593	23125	21271	20651	29739	33649
Imax (mm4)	17405	18542	19943	16166	16784	13934	24944	31079	28019	15742	14528	15583	21679	24966
Imin (mm4)	6649	8059	8134	6933	7008	5007	9282	22141	7574	7382	6743	5068	8060	8684
ToD (mg/cm3)	220.6	206.2	230.6	172.0	236.6	290.5	226.0	238.4	275.6	231.8	312.1	211.3	376.4	240.5
ToA (mm2)	365.8	403.7	401.0	389.1	368.6	326.4	439.7	588.0	408.0	385.0	357.3	371.5	398.6	426.6
BSIc (g2/cm4)	0.17795	0.17160	0.21319	0.11505	0.20637	0.27539	0.22465	0.33417	0.30993	0.20683	0.34794	0.16585	0.56478	0.24662
ToC [g/cm]	0.807	0.832	0.925	0.669	0.872	0.948	0.994	1.402	1.125	0.892	1.115	0.785	1.500	1.026
CoC [g/cm]	0.049	0.174	0.158	0.018	0.094	0.499	0.171	0.183	0.264	0.098	0.332	0.233	0.431	0.223

With regards to the first objective of model development, a x_{arm} value of 0.91 mm provided the highest correlation linking experimental failure load with BSI_M ($R^2 = 0.90$) and BSI_L ($R^2 = 0.86$). A y_{arm} value of 0.03 mm provided the highest correlation with BSI_V and BSI_D ($R^2 = 0.88$). These values were chosen for contrasting the new models against previous imaging measures used to predict failure load. Scatter plots with the regression equation for each parameter and coefficient of determination (R^2) for BSI_M, BSI_L, BSI_V and BSI_D linking predicted values with experimental failure load can be found in Figure 4.1 - Figure 4.4.

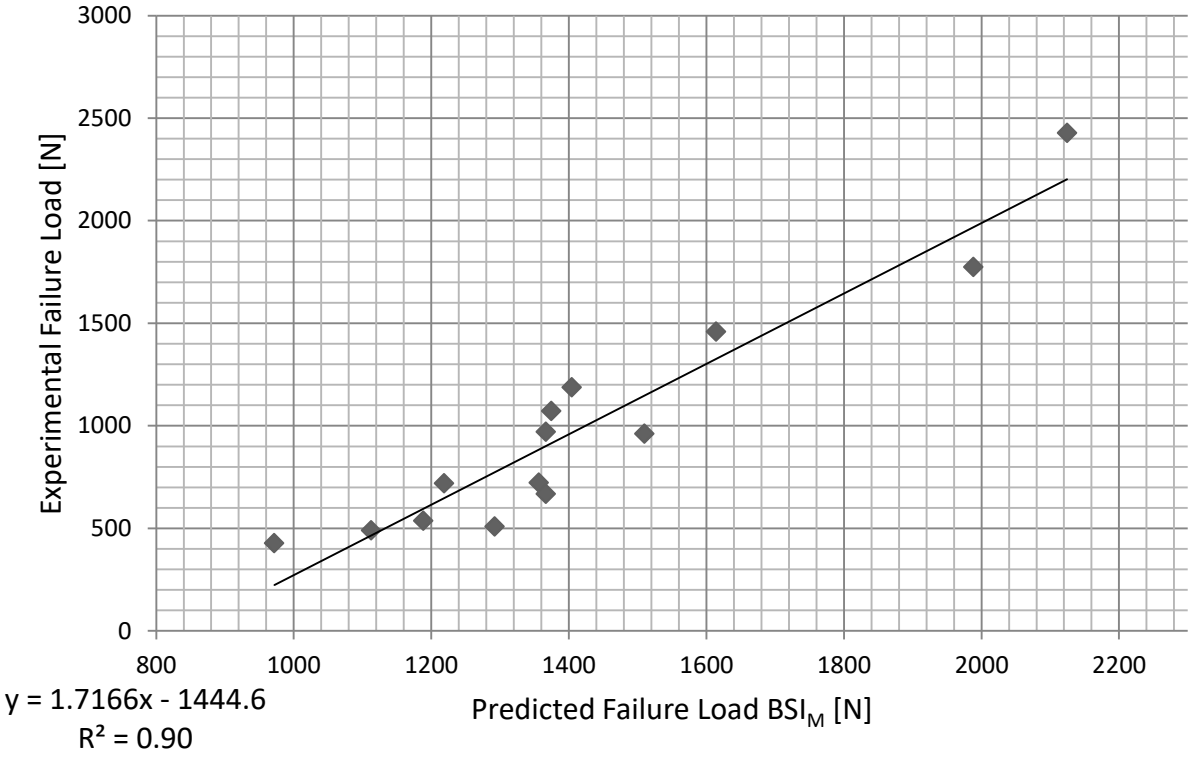

Figure 4.1: Experimental vs. Predicted Failure Load from BSI_M

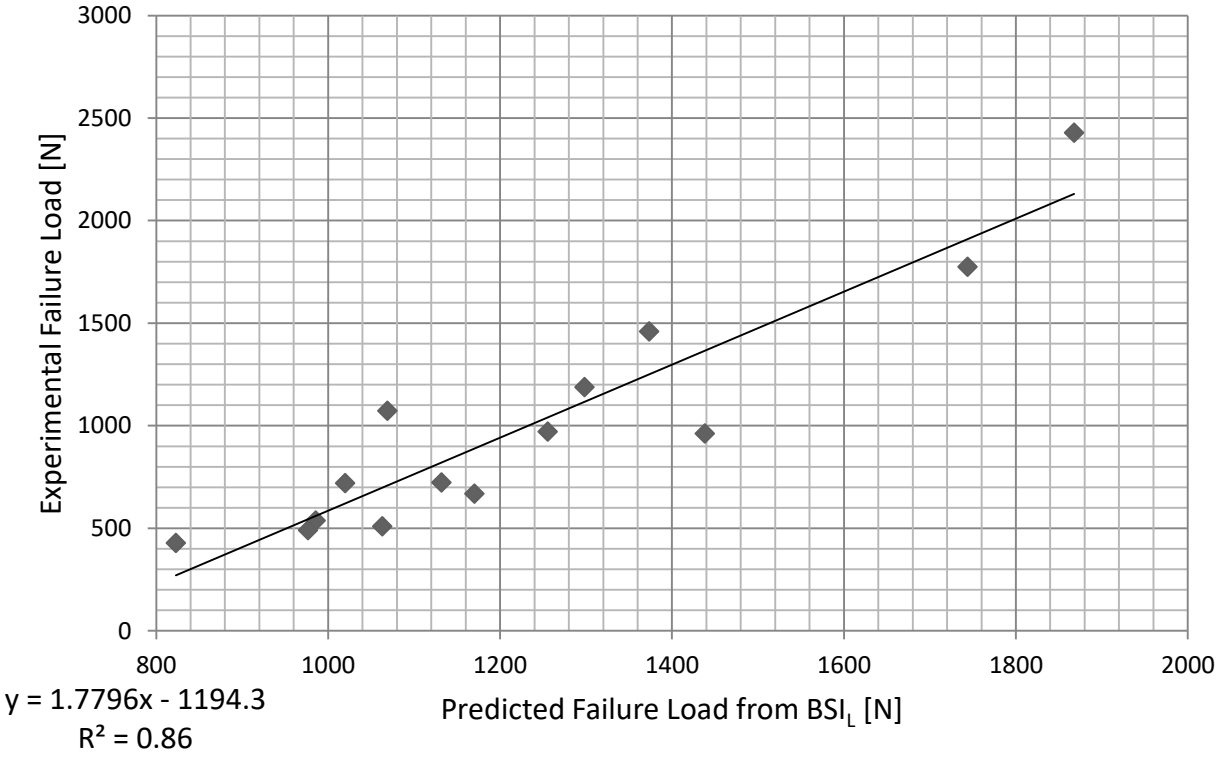

Figure 4.2: Experimental vs. Predicted Failure Load from BSI_L

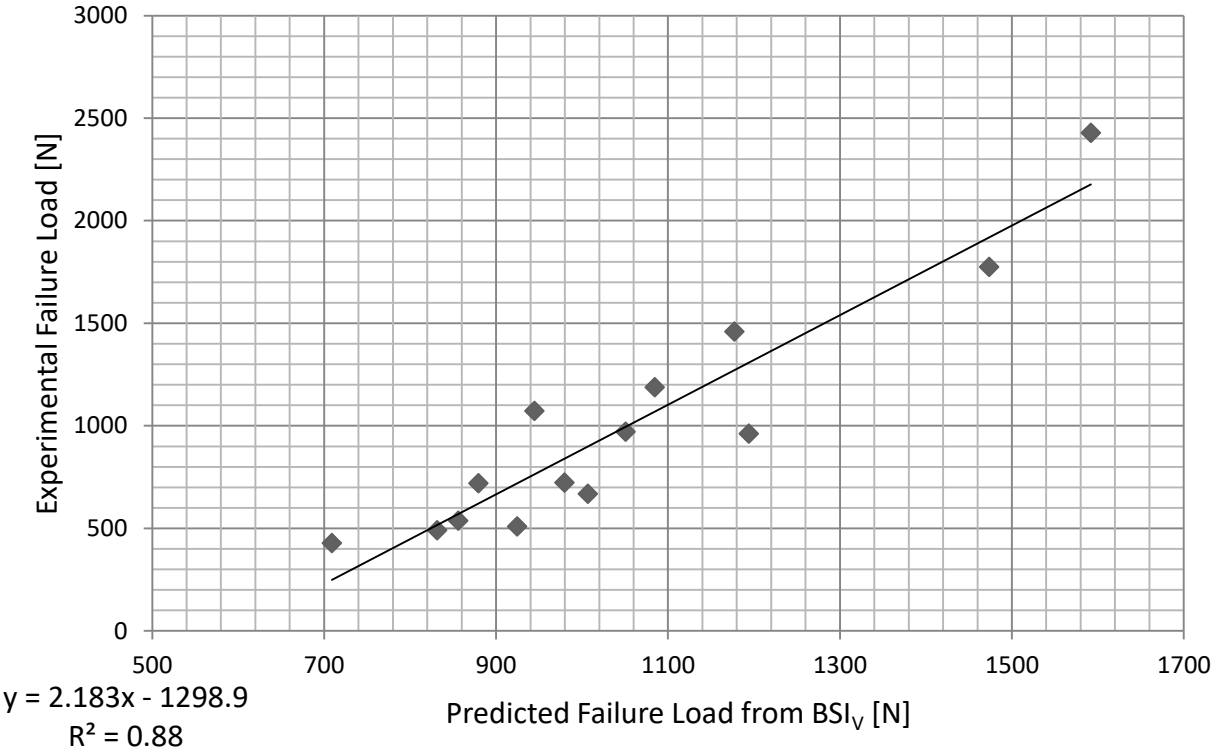

Figure 4.3: Experimental vs. Predicted Failure Load from BSI_V

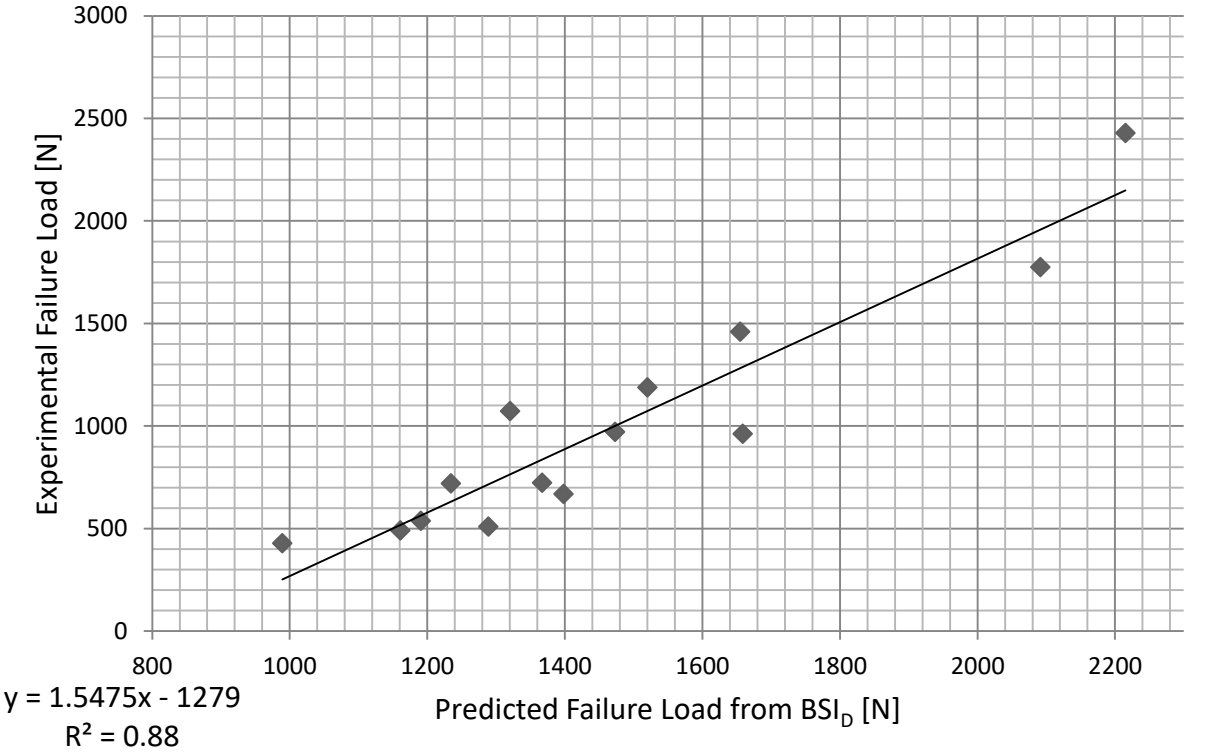

Figure 4.4: Experimental vs. Predicted Failure Load from BSI_D

Table 4.3: Linear regression coefficients of determination (R^2) between experimentally measured failure load and image-based estimates of failure load

Metric	R^2
CoD [mg/cm^3]	0.12
ToA [mm^2]	0.20
I_{max} [mm^4]	0.21
I_{min} [mm^4]	0.23
I_p [mm^4]	0.25
CoC [g/cm]	0.24
CoA [mm^2]	0.27
SSI_{min} [mm^3]	0.52
ToD [mg/cm^3]	0.57
SSI_{max} [mm^3]	0.71
SSI_p [mm^3]	0.73
BSI_c [g/cm^4]	0.83
BSI_L [N]	0.86
ToC [g/cm]	0.88
BSI_V [N]	0.88
BSI_D [N]	0.88
BSI_M [N]	0.90

5. Discussion

Many of the coefficients of determination from this work fit into the range of previously published values which used the same loading configuration (Table 2..1). ToD is the most commonly used measure for predicting ultimate failure load. This study found that it provided a moderately successful predictor ($R^2 = 0.57$); however, it may be possible to improve upon this performance with measures that include bone geometry. Interestingly, CoD was not a suitable predictor of ultimate load ($R^2 = 0.12$) ($P > 0.05$). ToA was not a predictor of ultimate load ($R^2 = 0.20$) ($P > 0.05$). This is likely because, as noted earlier, total area includes cortical bone, trabecular bone as well as bone marrow within its value even though trabecular bone and cortical bone take different amounts of load [47]; however, in the ToA measure, each pixel is assumed to share load equally. Unlike ToA, CoA had a coefficient of determination related to ultimate failure load which was significantly different than the null hypothesis ($R^2 = 0.27$) ($P < 0.05$). This change may be because cortical bone carries much more of the load than trabecular bone. These area measures are not weighted by density once they are past the minimum threshold to be included. By excluding the large amount of trabecular load, it appears that cortical area is able to provide a more accurate method of predicting ultimate load.

The area moment of inertia in the volar-dorsal direction, I_{max}, showed a low coefficient of determination 0.21. This value was found to not be significant ($P > 0.05$). I_{max} was also found not to be significant in Muller et al. 2003, [18]. The area moment of inertia in the volar-dorsal direction, I_{min}, showed a small coefficient of determination as well ($R^2 = 0.23$). This value was also shown to not have significance for predicting the measured failure load ($P > 0.05$). The polar moment of inertia, I_p, also showed a coefficient of determination for predicting ultimate load ($R^2 = 0.25$) that was not significant ($P > 0.05$). SSI_{max}, the stress-strain index in the volar-dorsal direction, was found to have a significant value for coefficient of determination for explaining variance in the ultimate failure load ($R^2 = 0.71$). While both SSI_{max} and I_{max} are measures of the capacity of the bone to resist bending in the same direction in the radius, the SSI_{max} considers that the higher density cortical bone will play more of a role in taking load than the less dense cortical while I_{max} does not make that distinction. This study found this to be the case as SSI_{min} showed a significant coefficient of determination ($R^2 = 0.52$) while I_{min} did not. The stress-strain index in the polar direction, SSI_p, is the summation of the SSI_{max} and SSI_{min}. While it is a resistance to torsional loading, it has been reported in the literature more frequently than SSI_{max}

or SSI_{min}. This work found the associated coefficient of determination to be 0.73. This had been one of the most successful predictors in previous studies for predicting ultimate experimental failure load [18].

The bone strength index in compression, BSI_c, showed a high coefficient of determination ($R^2 = 0.83$) for predicting failure load. These results are similar to previous findings at the distal tibia which found an R^2 of 0.85 linking BSI_c with distal tibia failure load [37]. These results validate usage of BSI_c as a failure load predictor for the radius now as well. Total bone mineral content, ToC, had a high coefficient of determination to predict variance of failure load ($R^2 = 0.88$). This is because ToC is equivalent to the normalized area used in this study, and is an appropriate equivalent of the area which carries load. ToC works as a measure of area that avoided pores, which would leave only the area which would transfer forces measured. ToC had also provided the strongest predictor in a previous study ($R^2 = 0.86$) [29]. ToC serves as an attempt to improve upon ToD by accounting for ToA as well. Unlike ToC, Cortical bone mineral content, CoC, was not a significant predictor of variance in ultimate load ($R^2 = 0.24$) ($P > 0.05$).

5.1. Bone Strength Index in Lateral Direction - BSI_L

BSI_L, is a novel method to assess ultimate load based on composite beam theory and combined loading reflective of a fall onto the outstretched hand. This study found that BSI_L had a maximum coefficient of determination of 0.86.

5.2. Bone Strength Index in Volar Direction - BSI_V

BSI_V is another novel method developed in this study to account for tensile bending stress applied to the furthest point on the volar side of the radius during a fall onto an outstretched hand. The index represents axial compression by using the same variables as ToC but also brings in a bending term due to an offset to the line of action, y_{arm}. This y_{arm} was found by maximizing the coefficient of determination for predicting ultimate failure load. The value for y_{arm} was found to be only 0.03 mm and including this bending term did not increase the maximum R^2 value from 0.88 from ToC. This indicates that bending did not have much effect in this direction.

5.3. Bone Strength Index in Dorsal Direction - BSI_D

BSI_D is similar to BSI_V except that it adds a term representing bending induced compressive stress to the term representing compressive stress from axial loading at the furthest point in the dorsal direction. As was discuss for BSI_V, bending did not contribute very much in this direction and the maximum R^2 value was the same as BSI_V and ToC ($R^2 = 0.88$).

5.4. Bone Strength Index in Medial Direction – BSI_M

BSI_M, is another novel method developed in this study to account for tensile bending in the medial-lateral direction present when falling onto the outstretched hand. This method had a significant coefficient of determination for predicting ultimate load ($R^2 = 0.90$) with a larger offset ($x_{arm} = 0.91$ mm) which showed bending had more of an effect in this direction than in the volar-dorsal direction.

5.5. Summary

The bending stresses considered as part of the off-axis loading moderately improved the predictive abilities of this model relative to a purely axial model. BSI_M had the peak coefficient of determination of all the models in this study of 0.90.

The four models developed in this study show a high coefficient of determination for predicting distal radius ultimate load during a fall scenario (BSI_L $R^2 = 0.86$, BSI_V & BSI_D $R^2 = 0.88$, BSI_M $R^2 = 0.90$). These values exceed those of other metrics taken from the literature. This indicates that these novel strength indices may serve as valuable tools to predict distal radius ultimate load from pQCT scans. Additionally, these results indicate that inclusion of bending effects may modestly improve failure load predictions.

5.6. Strengths and Limitations

5.6.1. Strengths

Strengths of this study pertain to usage of a realistic experimental loading configuration, inclusion of bending and axial loading, and model simplification. First, in this study the intact wrist was evaluated, which included the scaphoid, radius, ulna and supportive ligamentous structures, all of which contribute to creating bending in the radius. In comparison with ex vivo testing of excised radii, this approach helped ensure that testing replicated the in vivo situation as

closely as possible. Second, this model accounted for both bending and compression which was a novel approach compared to those found in the literature. Third, the recommended model is quite simple, and can be applied with existing data and existing bone outcomes. In comparison with subject-specific FE modeling, this approach takes very little time or specialized knowledge to calculate and apply.

5.6.2. Design Limitations

There are several important limitations arising from the design of this study. First, this study did not account for the ulna in the failure load assessment, although the ulna accounts for some of the load taken through the forearm during loading [52-54] and ulnar fractures can sometimes accompany distal radius fractures [48]. Second, the sample size consisted of both preserved (n=8) and fresh-frozen (n=6) specimens. The samples tested here were embalmed approximately 1 year prior to testing and differences due to this length of time have not been fully examined. When the two preservation types were examined separately it was determined that they had significantly different regression slopes and intercepts for all the novel indices. These differences show that a study may be more successful with only one preservation method across all samples. Third, some of the samples which were tested did not experience a Colles' fracture and were excluded from the analyses which limited the available sample size. Fourth, the donors for the samples here were quite aged, with the embalmed specimens being comprised of eight embalmed samples (four males, three females, one sex unknown) with a mean age of 73.4 years ± 8.3 years (range 56 - 81). The fresh-frozen samples were all from female donors with a mean age of 87.8 years ± 7.3 years standard deviation (range 79 - 101). This work would have benefited from having a range of ages and sexes represented in the sample selection to make the models more applicable to younger individuals. Even though not all ages are represented, postmenopausal female patients are the most likely to suffer from a Colles' fracture [1] so these models are still applicable to the group at the greatest risk. Fifth, the hands were aligned in the mechanical testing machine to make the palm flat in order to try and keep the bending force in the medial-lateral direction negligible. This was done to replicate how a person would contact the ground during a fall. Inclusion of bending about the volar-dorsal axis (pertaining to SSI_{max}) may have improved failure load predictions which included only bending about the medial-lateral axis. Unfortunately, however, limited information is provided with ImageJ, BoneJ or the Stratec

software which allows inclusion of both SSI_{max} and SSI_{min}. This is because the two measures pertain to different points on the outer cortical periphery of bone. SSI_{max} is a weighted I_{max} divided by the maximum distance (in the medial-lateral direction) from the principal axis (which is directed volar-dorsal); whereas, SSI_{min} is a weighted I_{min} divided by the maximum distance (in the volar-dorsal direction) from the principal axis (which is directed medial-lateral). These maximum distances do not necessarily coincide. In order to combine the two measures, an SSI specific to specific coordinates is required, which requires custom coding beyond the scope of this thesis. Sixth, a flaw in the custom testing program caused a very brief pause at 100 N for all of the tests; although highly unlikely, this may have affected the measured yield and ultimate loads during mechanical testing.

5.6.3. Technical Limitations

Technical limitations arising during this research pertained to threshold determination and mechanical testing limits. First, it was difficult to identify appropriate threshold values for pQCT images during the image analysis in BoneJ. The minimum threshold for bone of 100 mg/cm^3 was chosen in order to include large interior regions within the bone which would otherwise be excluded; but, this also led to some small regions around the cortical shell being included which may have been erroneous. Second, testing was done at a rate of 180 mm/min, which is slower than rates experienced during a fall onto the outstretched hand [49] but was similar to previous research [50]. For reference, two initial tests were (accidently) conducted at a rate of 10800 mm/min, but the fracture event was so sudden it was unclear whether the samples experienced a Colles' fracture as they were demolished beyond recognition. Finally, a linear relationship between Young's modulus and local bone mineral density was assumed but it has been shown a relation to the second power between the two parameters is more accurate at the tibia [23]; however, the relationship between the two varies by anatomical site [51].

6. Conclusions and Future Directions

6.1. Conclusions

The results of this study indicated that a novel tensile bone strength index for off-axis loading, BSI_M, can be used to predict failure load of the distal radius, with 90% explained variance, from a pQCT scan image taken at the 4% site of the radius with a 0.4 mm pixel size. Two other novel bone strength indices for off-axis loading, BSI_V and BSI_D, had coefficients of determination of 0.88. Additionally, BSI_L had a R^2 value of 0.86. The results of this study indicated that BSI_c explains 83% of the variance in failure load at the distal radius, which supports findings at the distal tibia, and thus validates its usage for modeling ultimate failulre load of the distal radius in a fall scenario.

Total bone mineral content, which is akin to a weighted area, was also found to have a coefficient of determination of 0.88 which exceeded the values in the literature for predicting ultimate load in the distal radius. Interestingly, I_{max}, I_{min}, I_p, ToA, CoC and CoD all exhibited coefficients of determination that were not significant ($P > 0.05$) with experimentally acquired failure loads and thus should not be employed as imaging-based estimates of distal radius failure load.

6.2. Contributions

There are various contributions arising from this research worthy of mention. First, results of this study indicate that inclusion of bending effects may modestly improve predictions of distal radius failure load. This new BSI_M method predicts variance in ultimate load up to 90% while BSI_V and BSI_D predict variance in ultimate load up to 88%. Although the improvements are modest (+2% relative to ToC), there is value in these findings. Also, the simplicity of these models makes them easy to implement with existing and previously acquired data. Second, this work found that ToC was a stronger predictor of ultimate failure load than the more commonly assessed density measures. This is important as many of the new generation tools (e.g., HR-pQCT, HR-pQCT II) have omitted ToC completely from their outcome measures in search of more advanced information such as trabecular thickness or cortical porosity. Although these other metrics are valuable for understanding longitudinal changes in growth, the main factor of interest should be bone's failure load, which is captured quite well by this simple measure. Third, the BSIc measure assessed in this study was able to explain 83% variance in failure load, which

mimics findings at the distal tibia of 85%. To date, BSIc has been employed to estimate distal radius failure load even though the method has only been validated at the distal tibia. These findings validate usage of the BSIc at the distal radius. Fourth, this study noted that many metrics were not able to predict distal radius failure load, even though they are widely employed in the literature. Caution should be exercised if attempting to employ I_{max}, I_{min}, I_p, ToA or CoD to estimate failure load.

6.3. Clinical Significance

The new models developed in this work could be used to predict ultimate failure load of the distal radius in vivo. This could be combined with predictions for impact load placed on the radius during a forward fall (based on height, weight and sex) in order to assess the fracture risk (via a safety factor) of a patient [6] in a clinical setting. These models could also be used to monitor the mechanical properties of bone for studies evaluating factors which affect bone failure load. For example, changes in bone failure load due to different activities, nutrition or medication could be examined with better accuracy by having a model which explains more variance in ultimate load. To summarize, this means that this new models could be used directly to assess ultimate load and could also be used to develop more effective methods to improve bone mechanical properties to lower the fracture risk of patients in danger of experiencing a Colles' fracture. Ultimately, this new tool may help to reduce the number of Colles' fractures occurring annually, which is expected to increase in the coming years as the population of elderly people increases [52].

6.4. Recommendations for Future Research

- Use a similar approach to develop new models which include the ulna in the BoneJ analysis of the pQCT scan images. This may provide a more effective model to predict ultimate load in the forearm since the ulna has been shown to take some of the load applied to the forearm during a fall [53].
- Develop similar models, which include both bending and axial effects, based on samples from younger adults or children. This would allow for studying the changes in ultimate load in the distal radius in these age groups. This could help to predict fracture risk or be utilized in studies examining factors which affect bone ultimate failure load.

- Developing models, based on principles, similar to those applied here, but with custom analyses instead of using outcomes derived directly from ImageJ, BoneJ or Stratec. Such a model could account for bending across both medial-lateral and dorsal-volar axes, in addition to axial compression, which should improve predictions of failure load. Such a model could also identify the local strength of bone (based upon strength being proportional to density squared [23] instead of using a constant value as has been done here).
- It would be prudent to evaluate this model with other sites such as the femur, with images acquired using MRI.
- Develop models where the ratio of maximum distances is left in variable form and is taken straight from the scan image may allow for wider applicability.
- Three tri-axial strain gauges were mounted on the radius and two linear gauges were mounted on the ulna during this testing but the strain data was not used in this study. All of the strain data for these tests was recorded at the same time as the load and displacement and this data could be used for determining an experimentally derived offset value for the bending moments which could also be done to validate the values found in this study.
- It may prove to be useful to investigate using all of the four bone strength indices and the use the predicted value of the lowest of the four and investigating that value in comparison to the failure load of the sample to see if it could improve the coefficient of determination over the individual models.

References

[1] J. A. Kanis, E. V. McCloskey, H. Johansson, A. Oden, L. J. Melton and N. Khaltaev, "A reference standard for the description of osteoporosis," *Bone,* pp. 467-475, 2008.

[2] R. Marcus, D. Feldman, D. W. Dempster, M. Luckey and J. A. Cauley, Osteoporosis, Waltham: Elsevier, 2013.

[3] P. Varga, D. H. Pahr, S. Baumbach and P. K. Zysset, "HR-pQCT based FE analysis of the most distal radius section provides an improved prediction of Colles' fracture load in vitro," *Bone,* pp. 982-988, 2010.

[4] K. L. Troy and M. D. Grabiner, "Off-axis loads cause failure of the distal radius at lower magnitudes than axial loads: A finite element analysis," *Journal of Biomechanics,* pp. 1670-1675, 2007.

[5] D. W. Wagner, D. P. Lindsey and G. S. Beaupre, "Replicating a Colles fracture in an excised radius: Revisiting testing protocols," *Journal of Biomechanics,* pp. 997-1002, 2012.

[6] C. E. Kawalilak, J. L. Lanovaz, J. D. Johnston and S. A. Kontulainen, "Linearity and sex-specificity of impact force prediction during a fall onto the outstretched hand using a single-damper model," *Journal of Musculoskeletal and Neuronal Interactions,* pp. 286-293, 2014.

[7] H. Gray and H. Carter, Gray's Anatomy, London: The Promotional Reprint Company Limited, 1991.

[8] F. Paulsen and J. Waschke, Sobotta: Atlas of Human Anatomy, Munich: Urban & Fisher Verlag, 2013.

[9] D. Sundh, D. Mellström, M. Nilsson, M. Karlsson, C. Ohlsson and M. Lorentzon, "Increased Cortical Porosity in Older Men With Fracture," *Journal of Bone and Mineral Research,* pp. 1692-1700, 2015.

[10] A. M. Parfitt, M. K. Drezner, F. H. Glorieux, J. A. Kanis, H. Malluche, P. J. Meunier, S. M. Ott and R. R. Recker, "Bone Histomorphometry: Standardization of Nomenclature, Symbols, and Units," *Journal of Bone and Mineral Research,* pp. 595-610, 1987.

[11] A. Colles, "On the Fracture of the Carpal Extremity of the Radius," *The Edinburgh Medical and Surgical Journal,* pp. 368-372, 1814.

[12] K. L. Troy and M. D. Grabiner, "Asymmetrical ground impact of the hands after a trip-induced fall: Experimental kinematics and kinetics," *Clincal Biomechanics,* pp. 1088-1095, 2007.

[13] D. T. Reilly and A. H. Burstein, "The Elastic and Ultimate Properties of Compact Bone Tissue," *Journal of Biomechanics,* pp. 393-405, 1975.

[14] R. B. Hopkins, N. Burke, C. Von Keyserlingk, W. D. Leslie, S. N. Morin, J. D. Adachi, A. Papaioannou, L. Bessette, J. P. Brown, L. Pericleous and J. Tarride, "The current economic burden of illness of osteoporosis in Canada," *Osteoporosis International,* pp. 3023-3032, 2016.

[15] World Health Organization, "Osteoporosis," 2007. [Online]. Available: http://www.who.int/chp/topics/Osteoporosis.pdf. [Accessed 27 October 2016].

[16] D. G. Seeley, W. S. Browner, M. C. Nevitt, H. K. Genant, J. C. Scott and S. R. Cummings, "Which fractures are associated with low appendicular bone mass in elderly women?," *Annals of Internal Medicine,* pp. 837-842, 1991.

[17] M. Cuddihy, S. Gabriel, C. Crowson, W. O'Fallon and L. Melton III, "Forearm Fractures as Predictors of Subsequent Osteoporotic Fractures," *Osteoporosis International,* pp. 469-475, 1999.

[18] M. E. Muller, C. E. Webber and M. L. Bouxsein, "Predicting the failure load of the distal radius," *Osteoporosis International,* pp. 345-352, 2003.

[19] E. -M. Lochmuller, J. Kristin, M. Matsuura, V. Kuhn, M. Hudelmaier, T. M. Link and F. Eckstein, "Measurement of Trabecular Bone Microstructure Does Not Improve Prediction of Mechanical Failure Loads at the Distal Radius Compared with Bone Mass Alone," *Calcified Tissue International,* pp. 293-299, 2008.

[20] J. N. Dowthwaite, R. M. Hickman, J. A. Kanaley, R. J. Ploutz-Snyder, J. A. Spadaro and T. A. Scerpella, "Distal Radius Strength: A Comparison of DXA-Derived vs pQCT-Measured Parameters in Adolescent Females," *Journal of Clincal Densitometry,* pp. 42-53, 2009.

[21] J. A. MacNeil and S. K. Boyd, "Accuracy of high-resolution peripheral quantitative computed tomography for measurement of bone quality," *Medical Engineering & Physics,* pp. 1096-1105, 2007.

[22] G. Guglielmi, I. Floriani, V. Torri, J. Li, C. Van Kuijk, H. K. Genant and T. F. Lang, "Effect of Spinal Degenerative Changes on Volumetric Bone Mineral Density of the Central Skeleton as Measured by Quantitative Computed Tomography," *Acta Radiologica,* pp. 269-275, 2005.

[23] D. R. Carter and W. C. Hayes, "The compressive behavior of bone as a two-phase porous structure," *The Journal of Bone and Joint Surgery,* pp. 954-962, 1977.

[24] B. Varghese, D. Short, R. Penmetsa, T. Goswami and T. Hangartner, "Computed-tomography-based finite-element models of long bones can accurately capture strain response to bending and torsion," *Journal of Biomechanics,* pp. 1374-1379, 2011.

[25] J. A. MacNeil and S. K. Boyd, "Bone strength at the distal radius can be estimated from high-resolution peripheral quantitative computed tomography and the finite element method," *Bone,* pp. 1203-1213, 2008.

[26] M. Hudelmaier, V. Kuhn, E. M. Lochmüller, H. Well, M. Priemel, T. M. Link and F. Eckstein, "Can geometry-based parameters from pQCT and material parameters from quantitative ultrasound (QUS) improve the prediction of radial bone strength over that by bone mass (DXA)?," *Osteoporosis International,* pp. 375-381, 2004.

[27] M. C. Ashe, K. M. Khan, S. A. Kontulainen, P. Guy, D. Liu, T. J. Beck and H. A. McKay, "Accuracy of pQCT for evaluating the aged human radius: an ashing, histomorphometry and failure load investigation," *Osteoporosis International,* pp. 1241-1251, 2006.

[28] Stratec Medizintechnik GmbH, "Technical Specifications," 19 March 2009. [Online]. Available: http://downloads.german-pavilion.com/downloads/pdf/exhibitor_19213.pdf. [Accessed 27 October 2016].

[29] P. Varga, E. Dall'Ara, D. H. Pahr, M. Pretterklieber and P. K. Zysset, "Validation of an HR-pQCT-based homogenized finite element approach using mechanical testing of ultra-distal radius sections," *Biomechanics and Modeling in Mechanobiology,* pp. 431-444, 2011.

[30] P. Augat, H. Reeb and L. E. Claes, "Prediction of Fracture Load at Different Skeletal Sites by Geometric Properties of the Cortical Shell," *Journal of Bone and Mineral Research,* pp. 1356-1363, 1996.

[31] E.-M. Lochmüller, C. A. Lill, V. Kuhn, E. Schneider and F. Eckstein, "Radius Bone Strength in Bending, Compression, and Falling and Its Correlation With Clinical Densitometry at Multiple Sites," *Journal of Bone and Mineral Research,* pp. 1629-1638, 2002.

[32] M. R. Bosisio, M. Talmant, W. Skalli, P. Laugier and D. Mitton, "Apparent Young's modulus of human radius using inverse finite-element method," *Journal of Biomechanics*, pp. 2022-2028, 2007.

[33] D. C. Newitt, S. Majumdar, B. van Rietbergen, G. von Ingersleben, S. T. Harris, H. K. Genant, C. Chesnut, P. Garnero and B. MacDonald, "In Vivo Assessment of Architecture and Micro-Finite Element Analysis Derived Indices of Mechanical Properties of Trabecular Bone in the Radius," *Osteoporosis International*, pp. 6-17, 2002.

[34] S. M. Nazemi, M. Amini, S. A. Kontulainen, J. S. Milner, D. W. Holdsworth, B. A. Masri, D. R. Wilson and J. D. Johnston, "Prediction of local proximal tibial subchondral bone structural stiffness using subject-specific finite element modeling: Effect of selected density-modulus relationship," *Clinial Biomechanics*, pp. 703-712, 2015.

[35] Y. Hasegawa, P. Schneider and C. Reiners, "Age, sex, and grip strength determine architectural bone parameters assessed by peripheral quantitative computed tomography (pQCT) at the human radius," *Journal of Biomechanics*, pp. 497-503, 2001.

[36] K. Crockett, C. M. Arnold, J. P. Farthing, P. D. Chilibeck, J. D. Johnston, B. Bath, A. D. G. Baxter-Jones and S. A. Kontulainen, "Bone strength and muscle properties in postmenopausal women with and without a recent distal radius fracture," *Osteoporosis International*, pp. 2461-2469, 2015.

[37] S. A. Kontulainen, J. D. Johnston, D. Liu, C. Leung, T. R. Oxland and H. A. McKay, "Strength indices from pQCT imaging predict up to 85% of variance in bone failure properties at tibial epiphysis and diaphysis," *Journal of Musculoskeletal & Neuronal Interactions*, pp. 401-409, 2008.

[38] F. Eckstein, E.-M. Lochmüller, C. A. Lill, V. Kuhn, E. Schneider, G. Delling and R. Müller, "Bone Strength at Clinically Relevant Sites Displays Substantial Heterogeneity and is Best Predicted From Site-Specific Bone Densitometry," *Journal of Bone and Mineral Research*, pp. 162-171, 2002.

[39] C. Öhman, E. Dall'Ara, M. Baleani, S. Van Sint Jan and M. Vicevonti, "The effects of embalming using a 4% formalin solution on the compressive mechanical properties of human cortical bone," *Clinical Biomechanics*, pp. 1294-1298, 2008.

[40] W. B. Edwards and K. L. Troy, "Simulating Distal Radius Fracture Strength Using Biomechanical Tests: A Modeling Study Examining the Influence of Boundary Conditions," *Journal of Biomechanical Engineering*, pp. 114501-1-114501-5, 2011.

[41] M. Doube, M. Kłosowski, I. Arganda-Carreras, F. Cordeliéres, R. Dougherty, J. Jackson, B. Schmid, J. Hutchinson and S. Shefelbine, "BoneJ; Free and extensible bone image analysis in ImageJ," *Bone*, pp. 1076-1079, 2010.

[42] E. F. Rybicki, F. A. Simonen, E. J. Mills, C. R. Hassler, P. Scoles, D. Milne and E. B. Weis, "Mathematical and experimental studies on the mechanics of plated transverse fractures," *Journal of Biomechanics*, pp. 377-384, 1974.

[43] C. A. Wigderowitz, C. R. Paterson, H. Dashti, D. McGurty and D. I. Rowley, "Prediction of Bone Strength from Cancellous Structure of Distal Radius: Can We Improve on DXA?," *Osteoporosis International*, pp. 840-846, 2000.

[44] D. R. Carter and D. M. Spengler, "Mechanical Properties and Composition of Cortical Bone," *Clinical Orthopaedics and Related Research*, pp. 192-217, 1978.

[45] J. C. Rice, S. C. Cowin and J. A. Bowman, "On the dependance of the elasticity and strength of cancellous bone on apparent density," *Journal of Biomechanics*, pp. 155-168, 1988.

[46] E. R. Myers, E. A. Sebeny, A. T. Hecker, T. A. Corcoran, J. A. Hipp, S. L. Greenspan and W. C. Hayes, "Correlations between photon absorption properties and failure load of the distal radius in vivo," *Calcified Tissue International*, pp. 292-297, 1991.

[47] J. A. MacNeil and S. K. Boyd, "Load distribution and the predictive power of morphological indices in the distal radius and tibia by high resolution peripheral quantitative computed tomography," *Bone*, pp. 129-137, 2007.

[48] M. Walz, B. Kolbow and G. Möllenhauf, "Fracture of the distal ulna accompanying fracture of the distal radius. Minimally invasive treatment with elastic stable intramedullary nailing," *Unfallchirurgie*, pp. 1058-1063, 2006.

[49] J.-S. Tan, J. J. Eng, S. N. Robinovitch and B. Warnick, "Wrist impact velocity are smaller in forward falls than backward falls from standing," *Journal of Biomechanics*, pp. 1804-1811, 2006.

[50] W. Pistoia, B. van Rietbergen, E.-M. Lochmüller, C. A. Lill, F. Eckstein and P. Rüegsegger, "Estimation of distal radius failure load with micro-finite element analysis models based on three-dimensional peripheral quantitative computed tomography images," *Bone*, pp. 842-848, 2002.

[51] E. F. Morgan, H. H. Bayraktar and T. M. Keaveny, "Trabecular bone modulus-density relationships depend on anatomic site," *Journal of Biomechanics,* pp. 897-904, 2003.

[52] P. Varga, S. Baumbach, D. Pahr and P. K. Zysset, "Validation of an anatomy specific finite element model of Colles' fracture," *Journal of Biomechanics,* pp. 1726-1731, 2009.

[53] H. Shaaban, G. Giakas, M. Bolton, R. Williams, P. Wicks, L. Scheker and V. Lees, "The load-bearing characteristics of the forearm: pattern of axial and bending force transmitted through the ulna and radius," *Journal of Hand Surgery,* pp. 274-279, 2006.

[54] K. L. Markolf, D. Lamey, S. Yang, R. Meals and R. Hotchkiss, "Radioulnar Load-Sharing in the Forearm. A Study in Cadavera," *The Journal of Bone & Joint Surgery,* pp. 879-888, 1998.

[55] M. F. Shepard, K. L. Markolf and A. M. Dunbar, "Effects of Radial Head Excision and Distal Radius Shortening on Load-Sharing in Cadaver Forearms," *The Journal of Bone & Joint Surgery,* pp. 92-100, 2001.

[56] K. A. Ward, J. E. Adams and T. N. Hangartner, "Recommendations for Thresholds for Cortical Bone Geometry and Density Measurement by Peripheral Quantitative Computed Tomography," *Calcified Tissue International,* pp. 275-280, 2005.

[57] S. P. Nielsen, X. Xie and O. Bärenholdt, "Geometric Properties of Distal Radius and Pathogenesis of Colles Fracture," *Journal of Clinical Densitometry,* pp. 209-219, 2001.

[58] L. Monfils, "Colles Fracture," February 2014. [Online]. Available: https://commons.wikimedia.org/wiki/File:Collesfracture.jpg. [Accessed 28 October 2016].

[59] A. Goel, "Colles' Fracture," 26 November 2015. [Online]. Available: https://radiopaedia.org/images/17712170. [Accessed 23 November 2016].

[60] A. Goel, "Colles' Fracture," 26 November 2015. [Online]. Available: https://radiopaedia.org/images/17712171. [Accessed 23 November 2016].

Appendix A - Mechanical Testing Raw Data

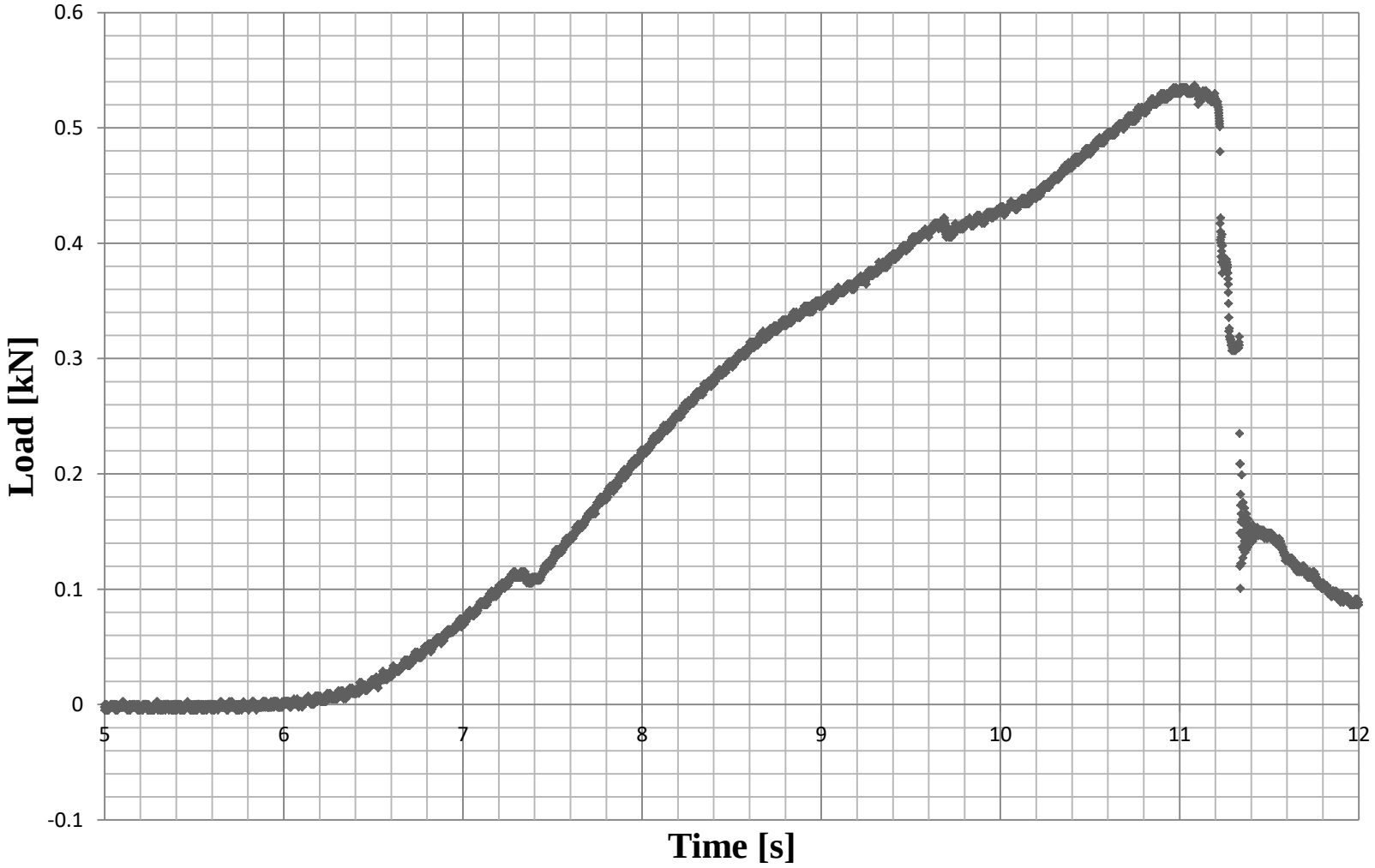

Figure A.1: Load versus Time Curve for Specimen 14-06029L

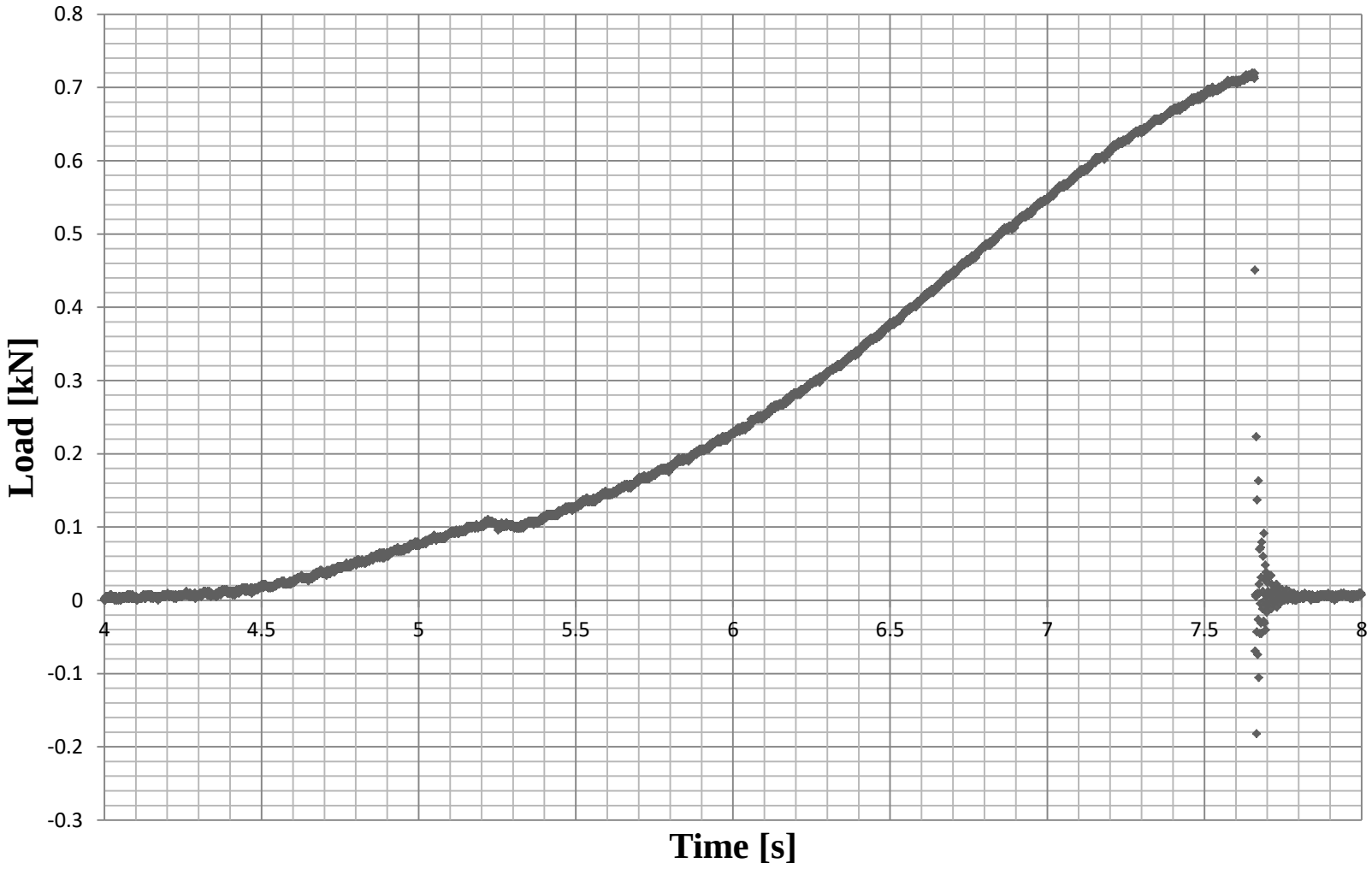

Figure A.2: Load versus Time Curve for Specimen 14-06059L

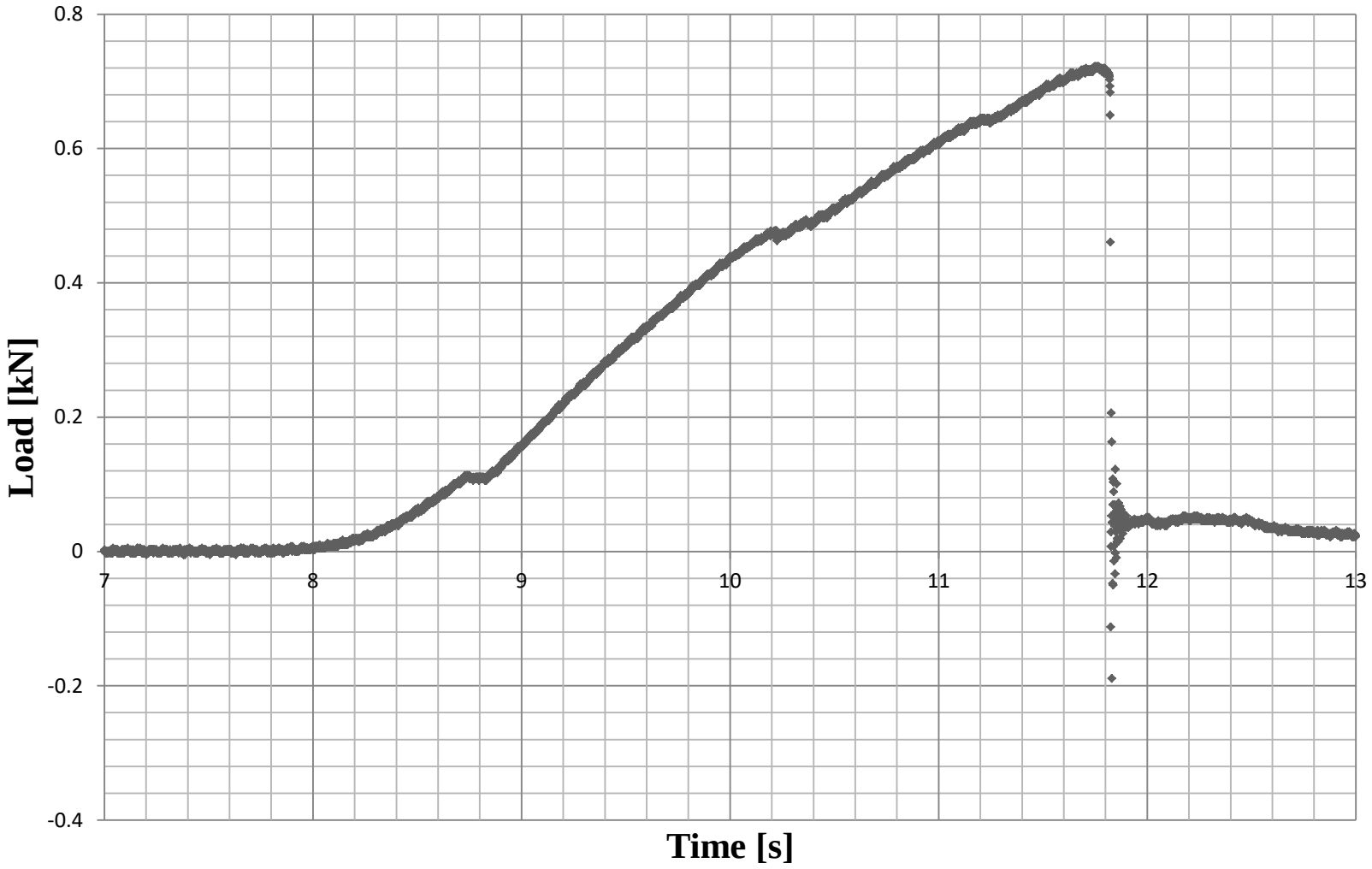

Figure A.3: Load versus Time Curve for Specimen 14-08067R

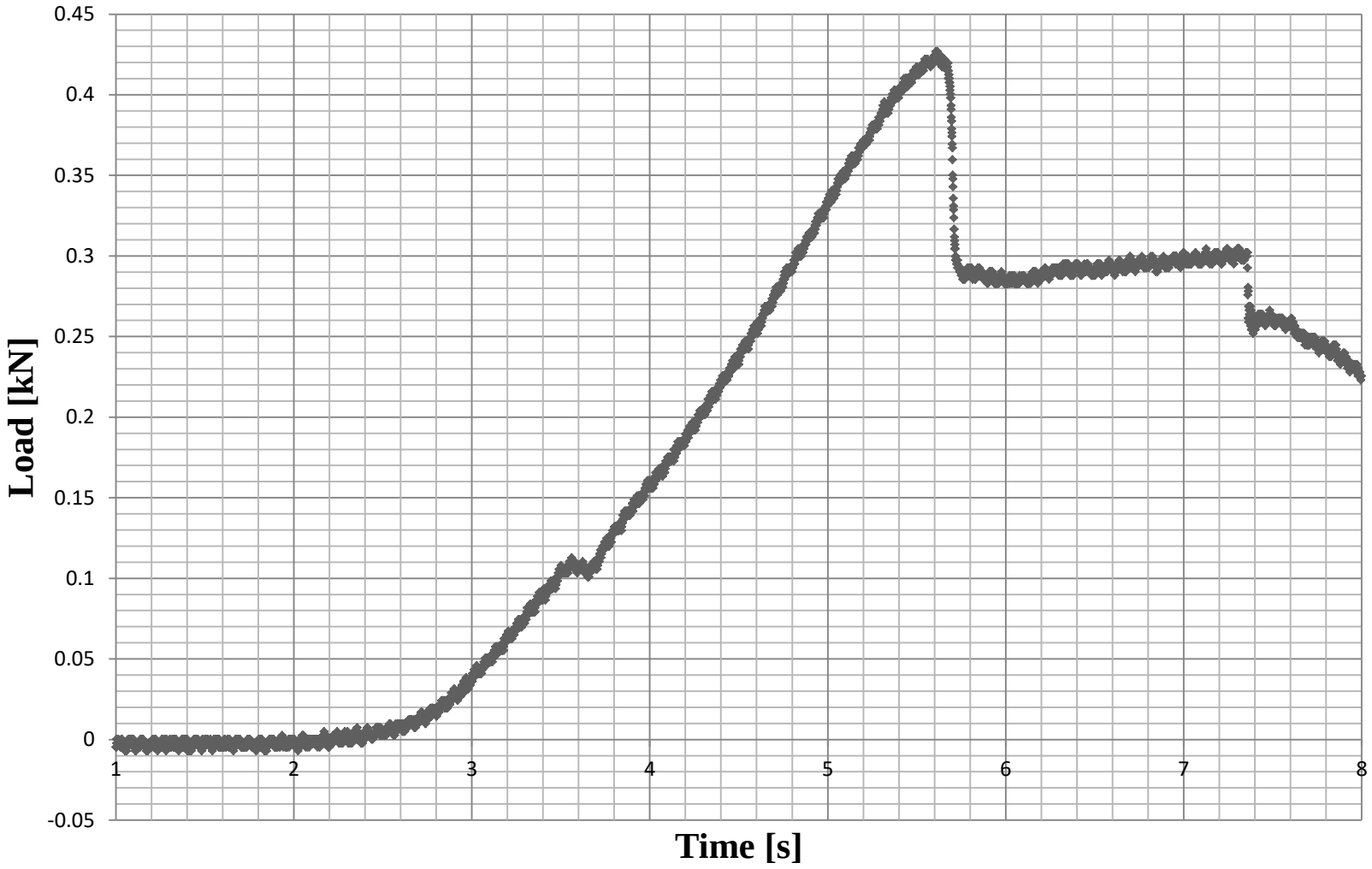

Figure A.4: Load versus Time Curve for Specimen 15-02039L

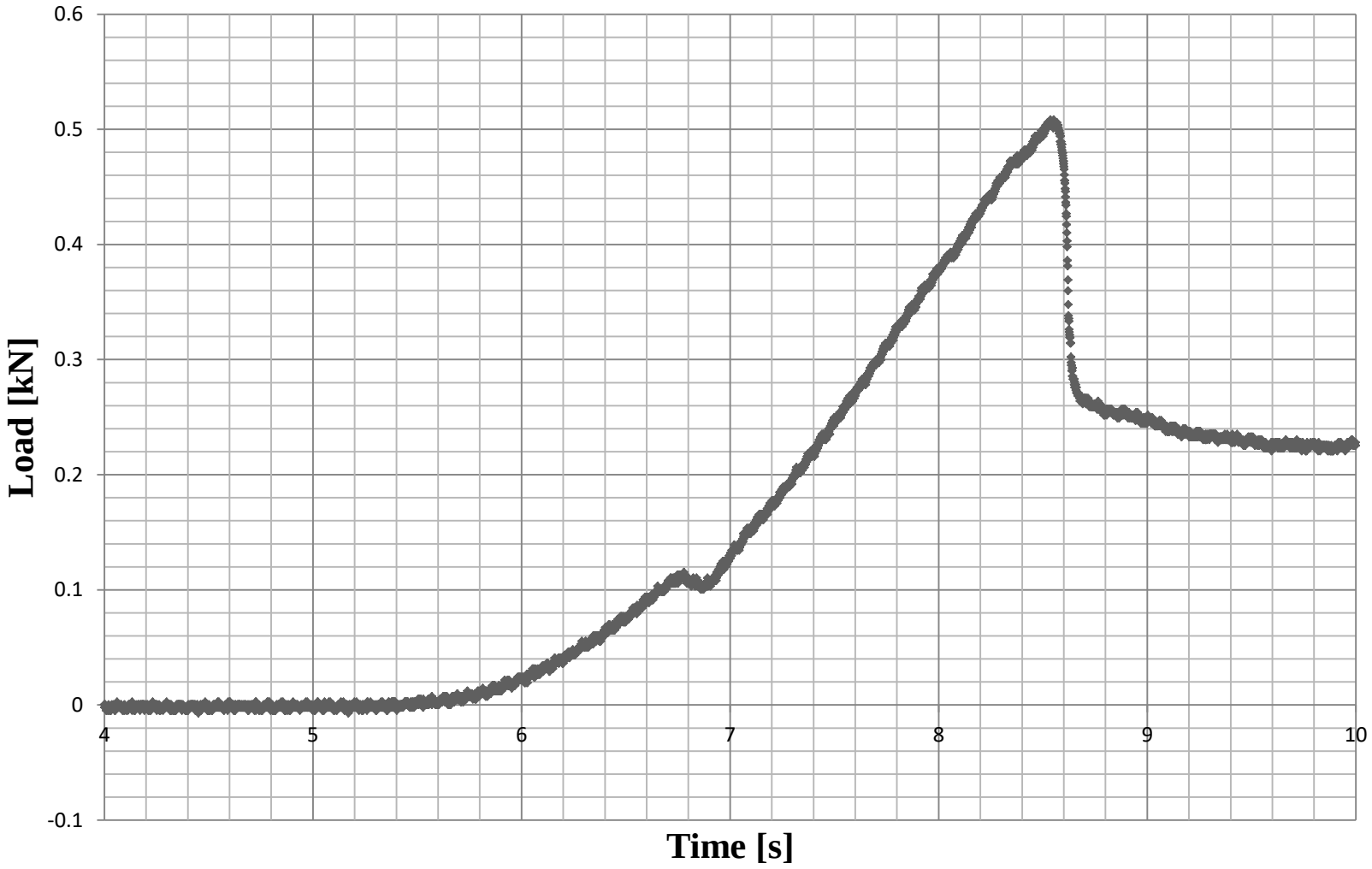

Figure A.5: Load versus Time Curve for Specimen 15-07012R

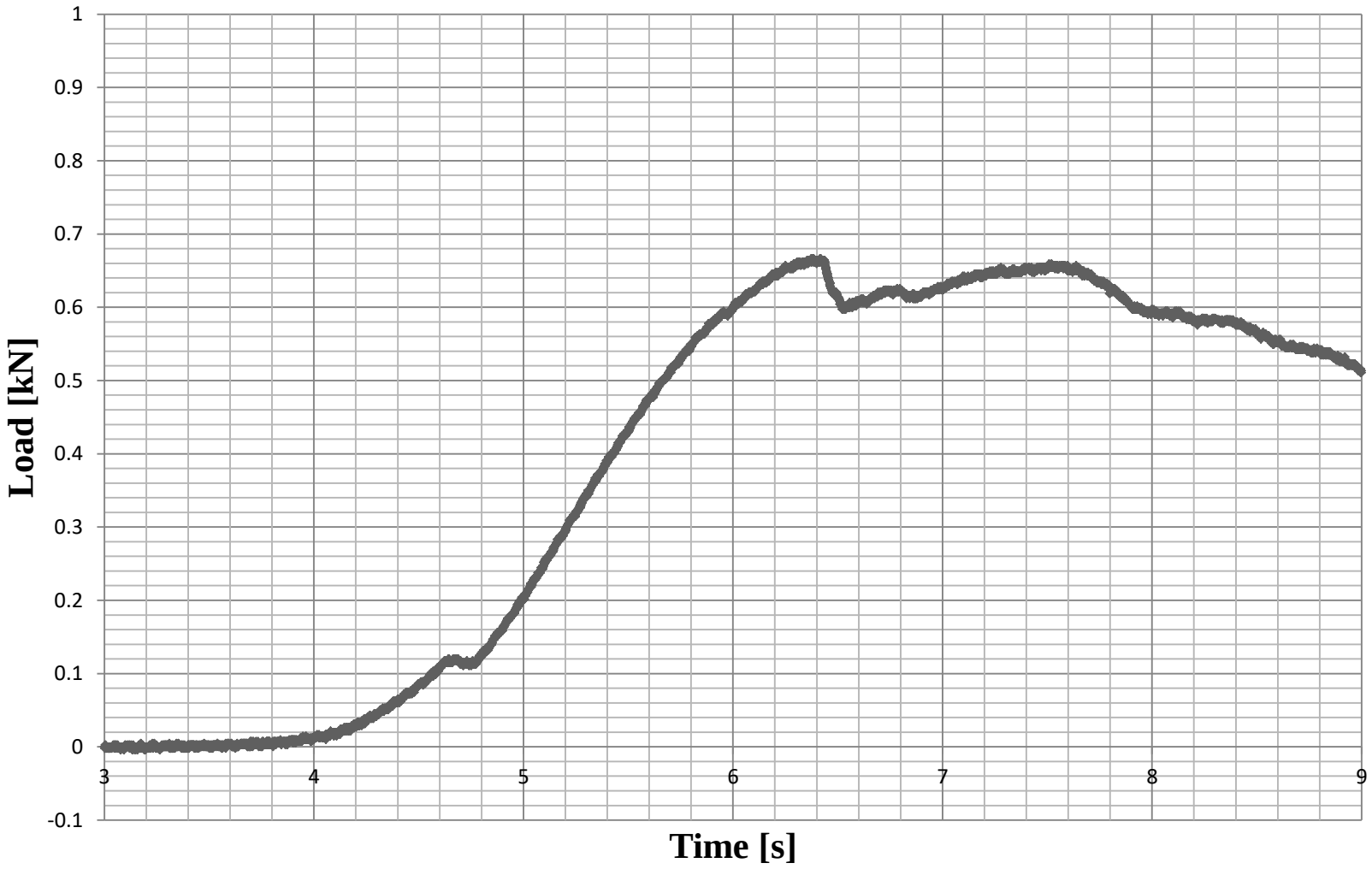

Figure A.6: Load versus Time Curve for Specimen 15-07037R

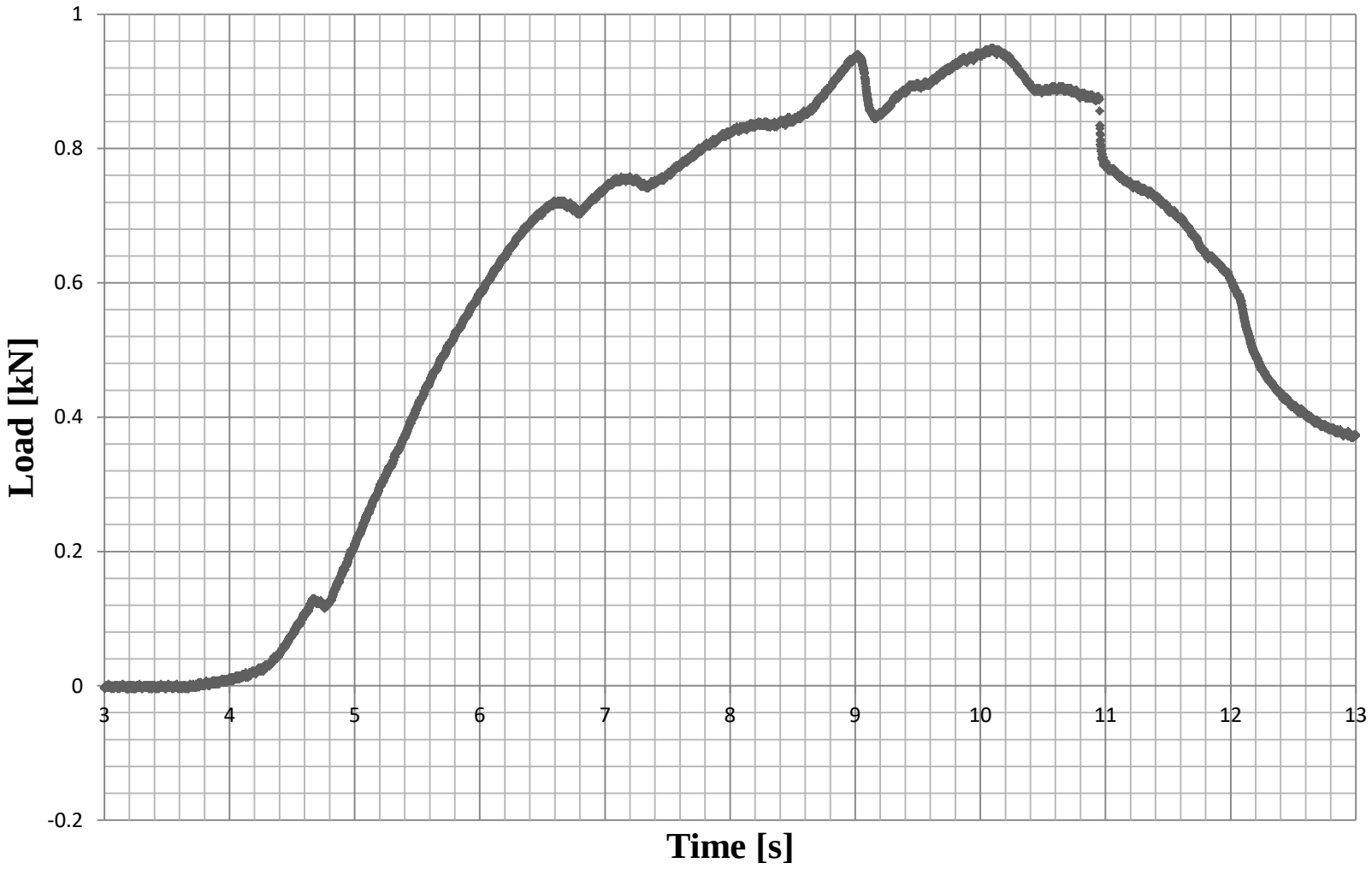

Figure A.7: Load versus Time Curve for Specimen 1538L

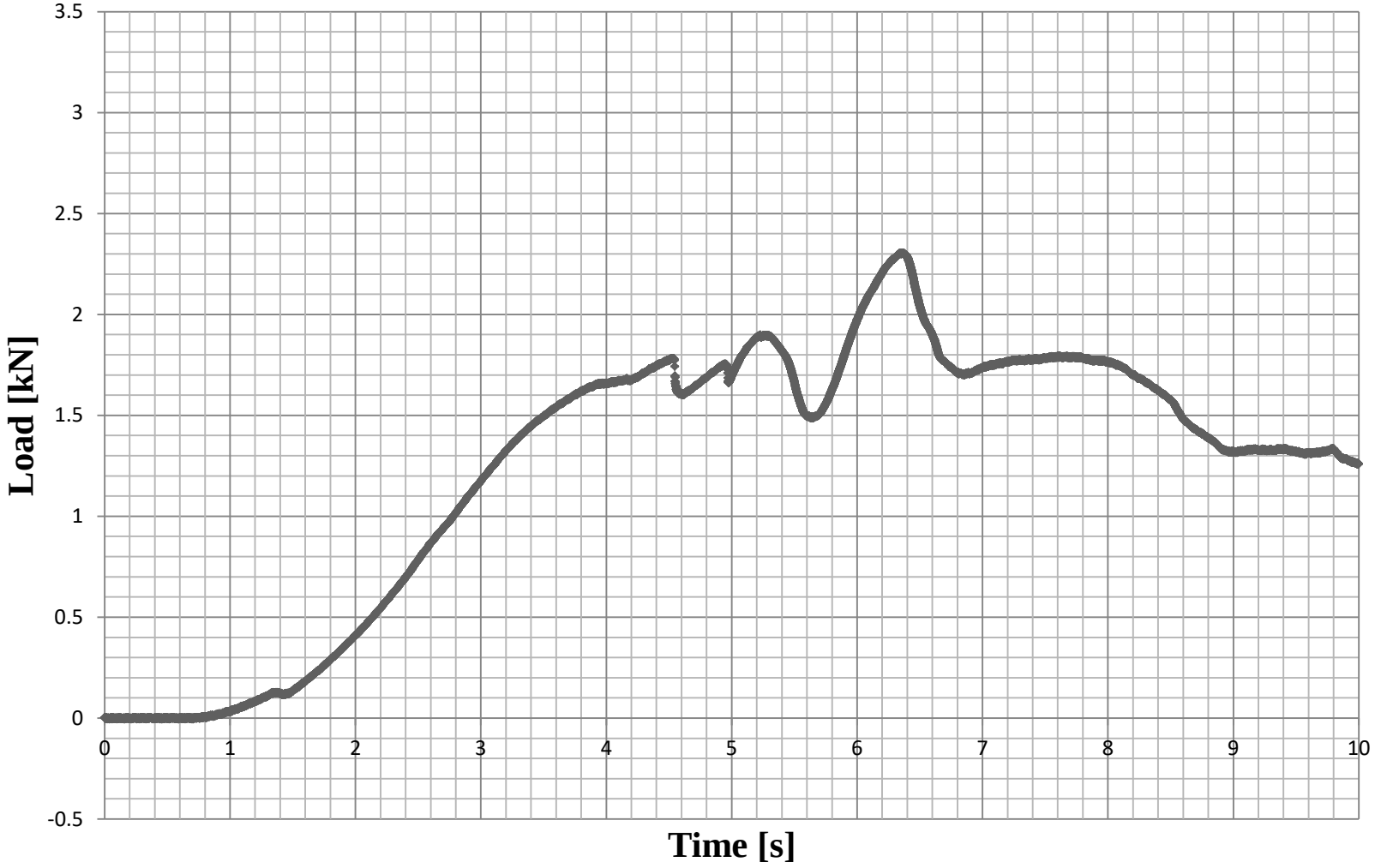

Figure A.8: Load versus Time Curve for Specimen 1539L

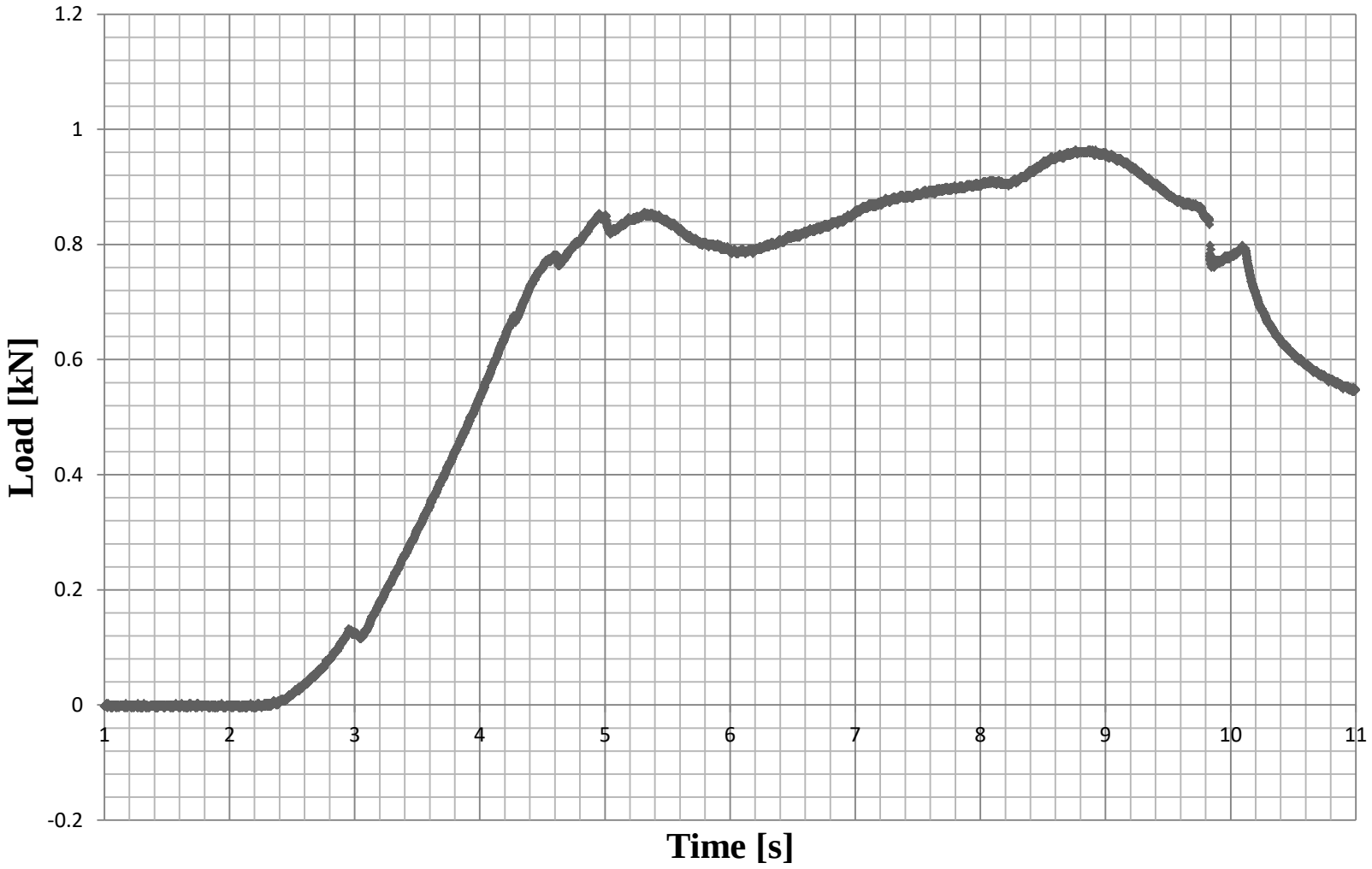

Figure A.9: Load versus Time Curve for Specimen 1546L

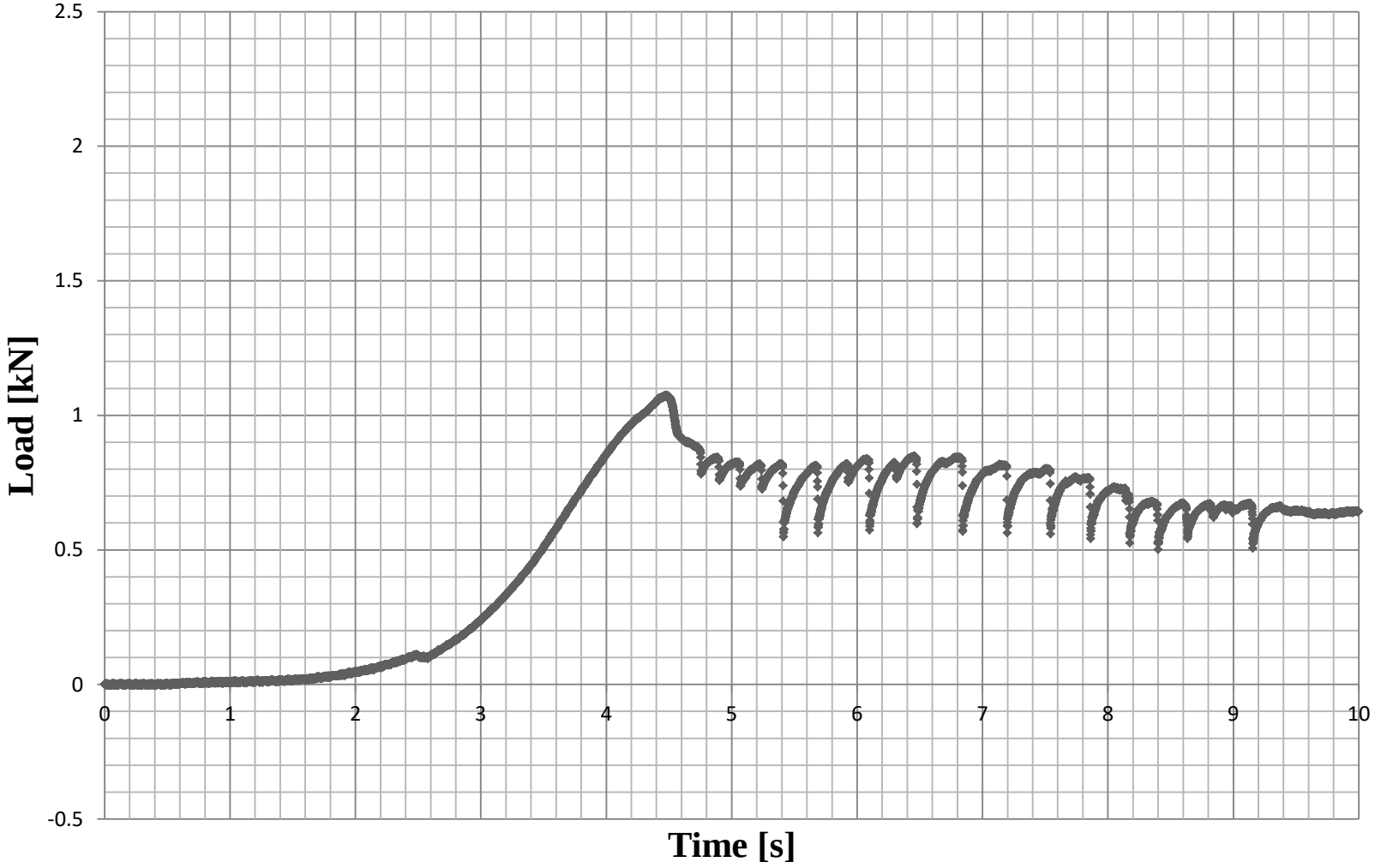

Figure A.10: Load versus Time Curve for Specimen 1561R

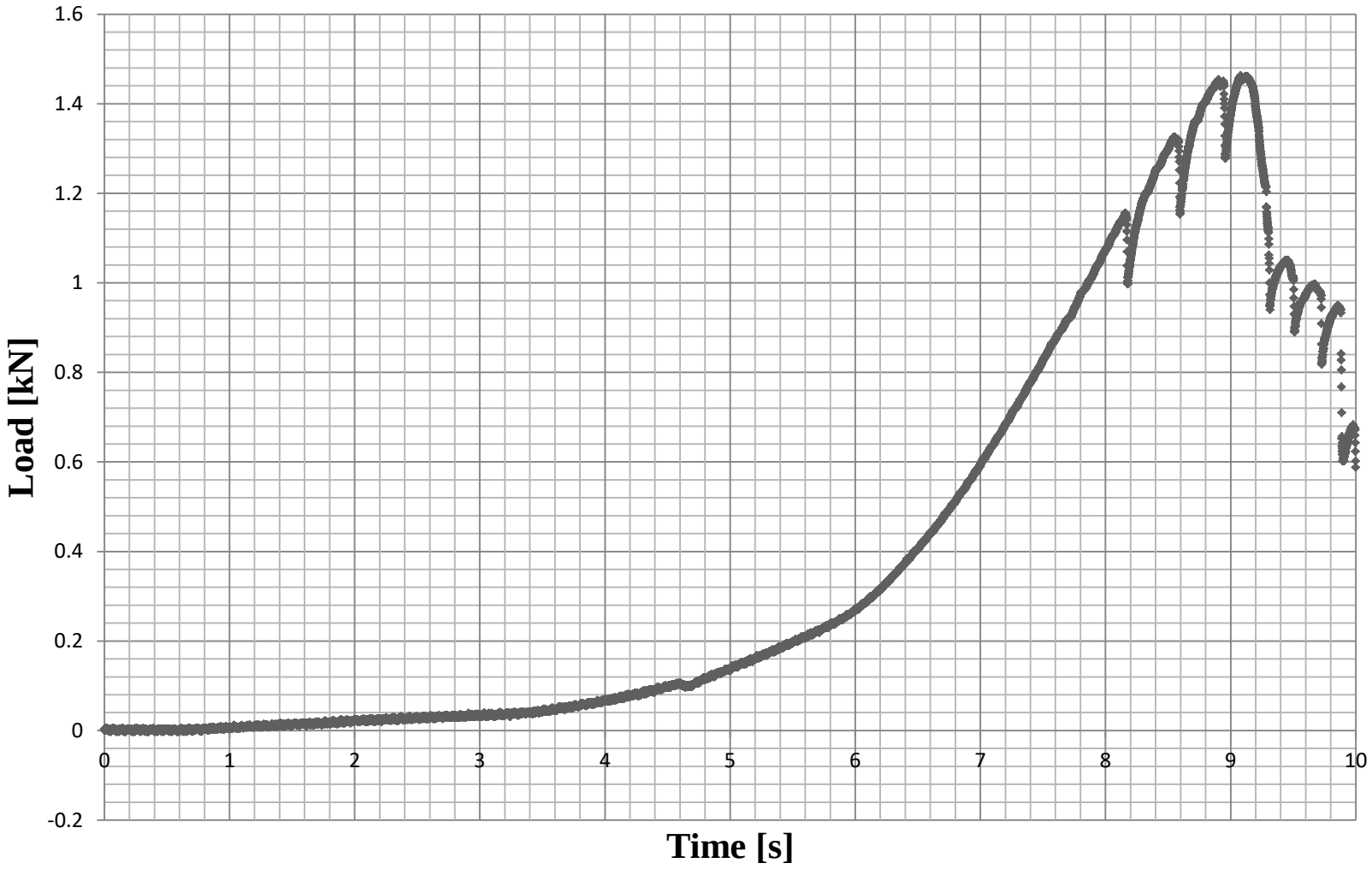

Figure A.11: Load versus Time Curve for Specimen 1564R

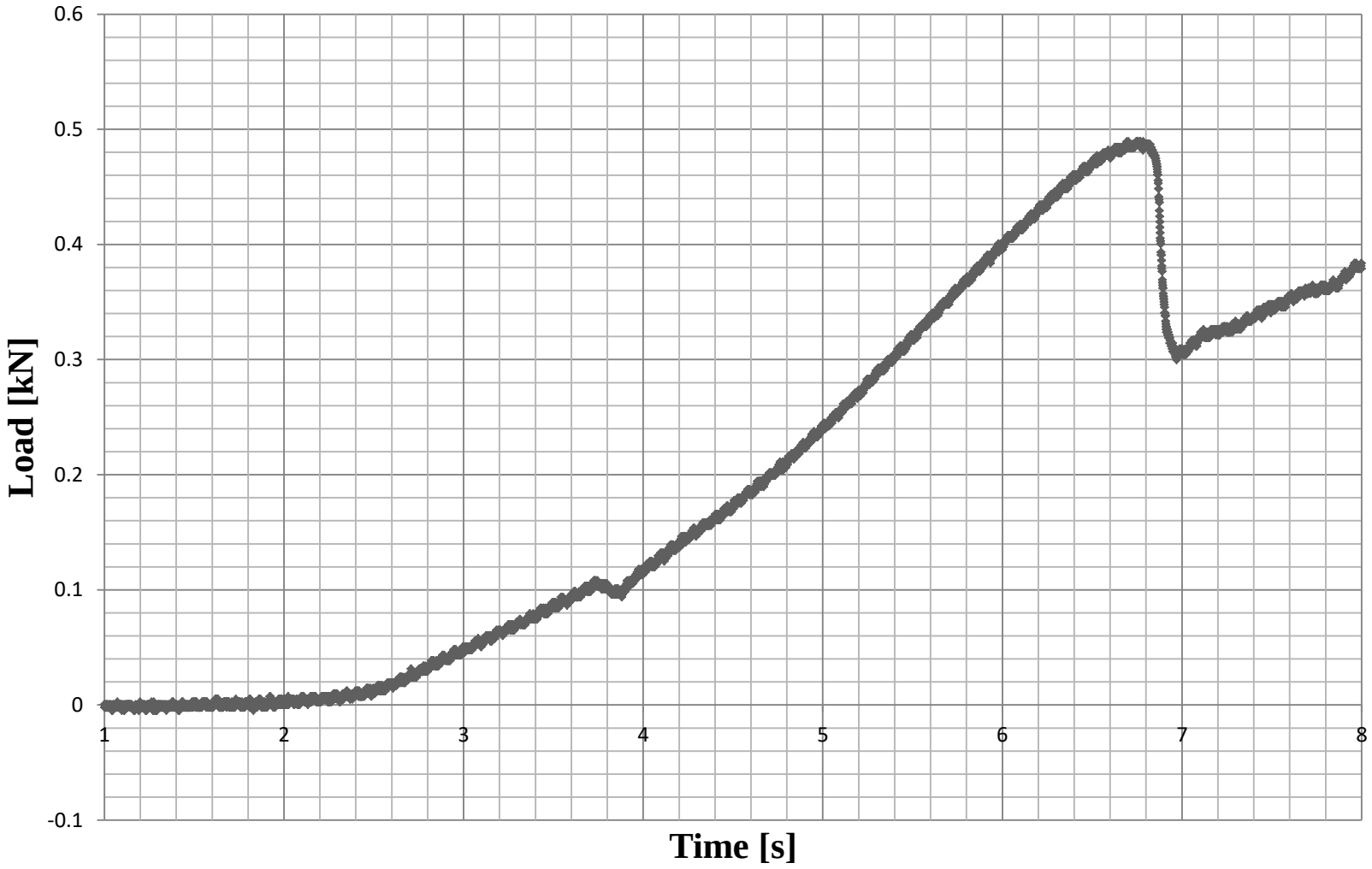

Figure A.12: Load versus Time Curve for Specimen 1567L

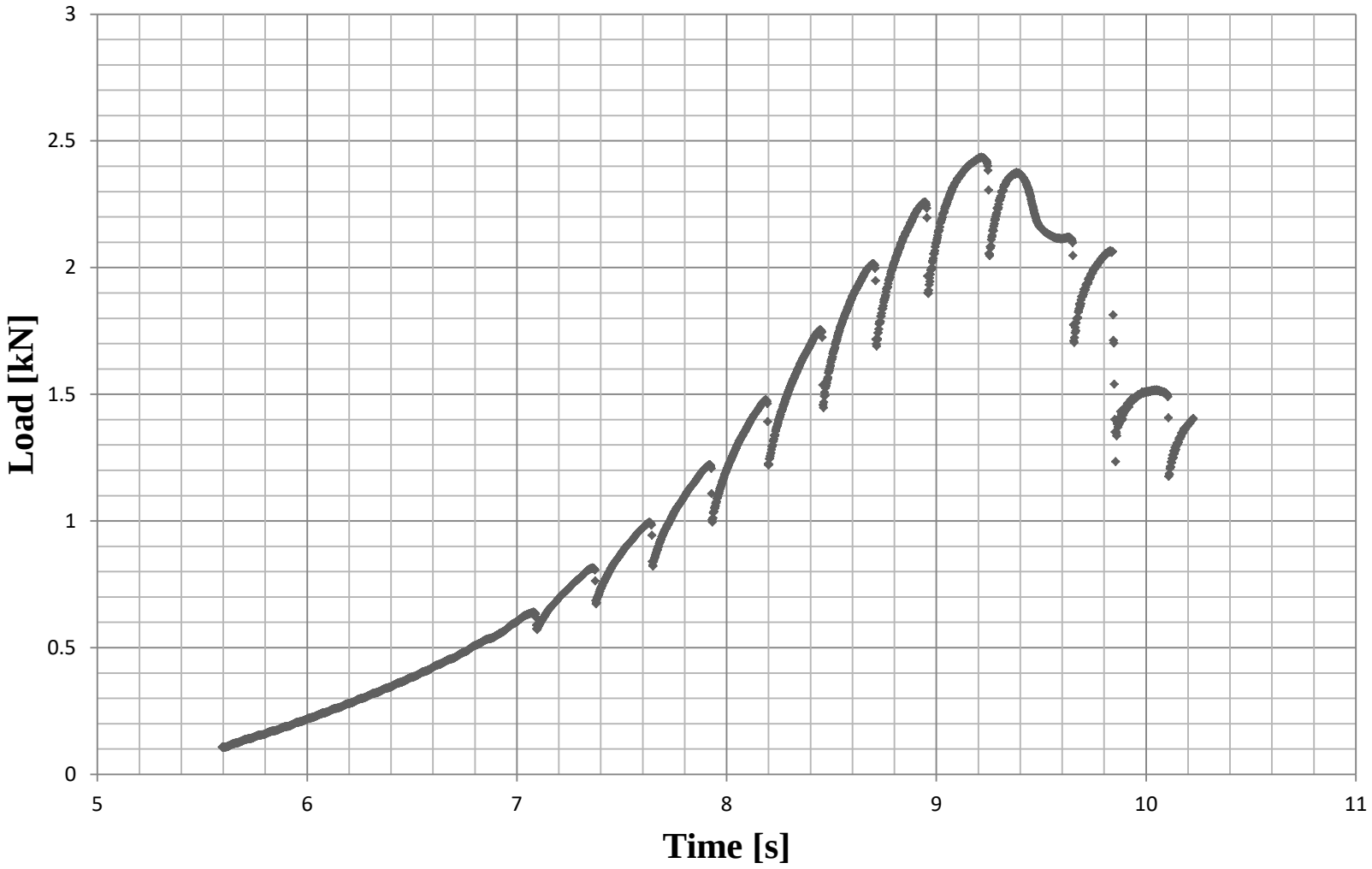

Figure A.13: Load versus Time Curve for Specimen 1568R

Note: Data taken from MTS Controller due to DAQ Crash during Test

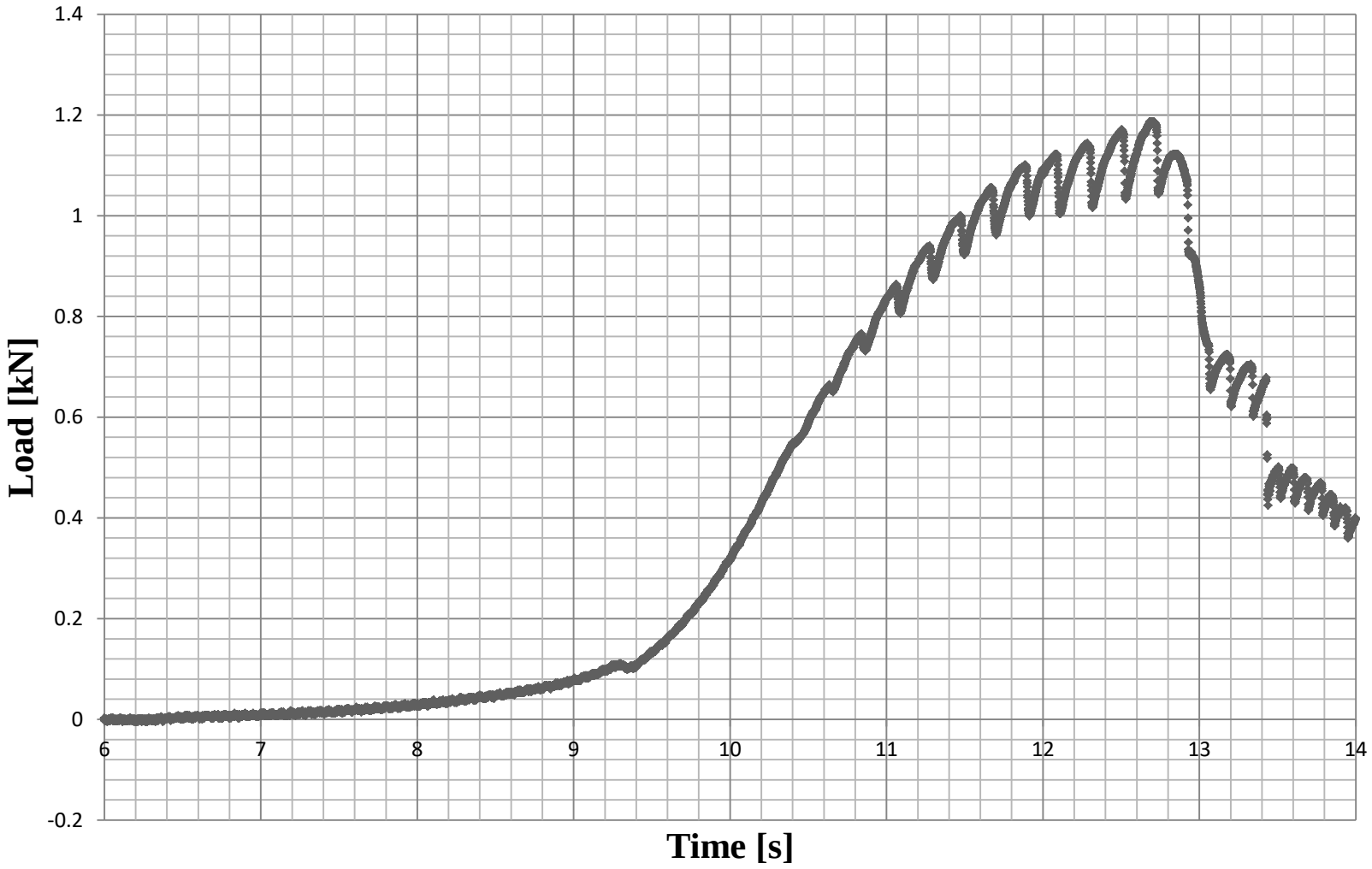

Figure A.14: Load versus Time Curve for Specimen BR

Appendix B - Strain Gauge Mounting Protocol

1.1. At the location marked for the pQCT scan site, remove soft tissue with a scalpel and then periosteum material by scraping edge of the scalpel along the surface where the gauges are to be applied. This should be on the volar, dorsal and lateral sides of the radius and on the dorsal and volar sides of the ulna. The gauge locations are highlighted in the image. In order to increase the speed of the application process, gauges 1 and 5 should have their adhesive layers applied at the same time to reduce total drying time and gauges 2-4 should also have their adhesive layers applied at the same time.

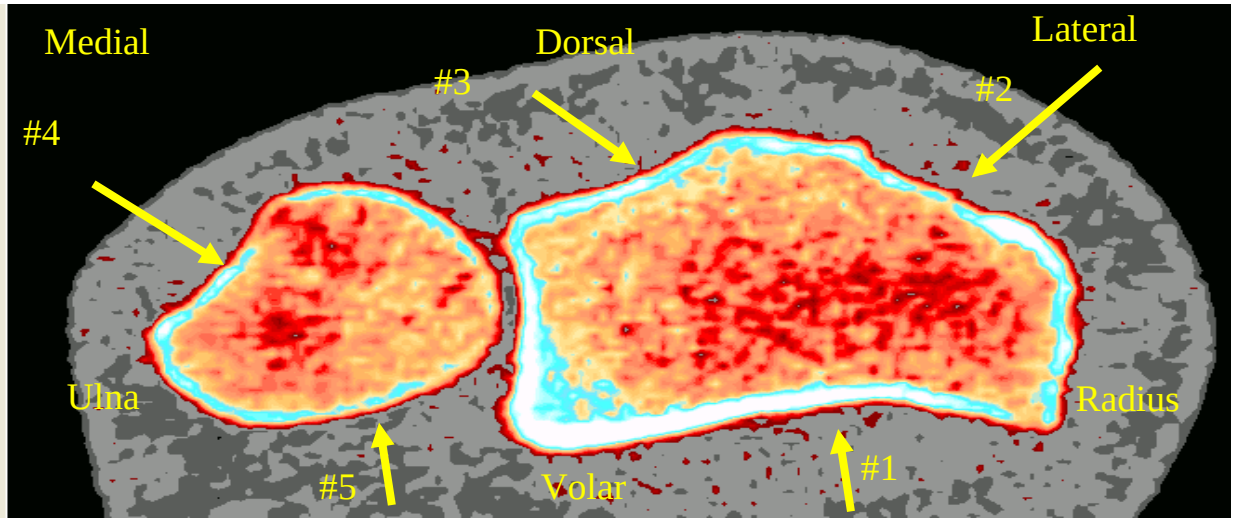

Figure B.1: Strain Gauge Mounting Locations

1.2. Clean surface with isopropyl alcohol wipe.

1.3. Sand surface using coarse grit sand paper.

1.4. Clean surface again with a new isopropyl alcohol wipe.

1.5. Sand surface with fine grit sand paper.

1.6. Place the back of each rosette on a piece of packing tape. Apply a small spot of Multi Mist Adhesive to the location where that gauge is to be mounted. Use a cotton swab to spread the adhesive over the entire area the gauge will require. Allow to dry completely

1.7. Apply a small spot of glue to a cotton swab and use it to apply glue to the back of the gauge. Ensure there is enough glue to cover the entire surface of the gauge, at this stage it is okay if there is a little bit of extra glue which is pushed out from underneath the gauge. While the extra will ensure that corners stay down better, it also means that the

adhesive will dry much slower so do not use too much. Position the gauge and apply pressure with a gloved finger. At this stage ensure the strain gauge is applied in the proper orientation. Only keep light finger pressure applied until the glue dries partially to prevent the glove being glued to the sample. Allow the glue to dry fully with no pressure.

1.8. If mounting gauges well in advance of testing: coat the back of the strain gauge with a thin layer of polyurethane to protect the gauge. Allow time to dry. If testing immediately, skip this step.

1.9. Wrap samples with damp paper towels and place back into storage bags unless testing immediately.